

1 | **On the forecast skills of a convection permitting ensemble**

2

3 THERESA SCHELLANDER-GORGAS¹, YONG WANG^{1*}, FLORIAN MEIER¹,
4 FLORIAN WEIDLE¹, CHRISTOPH WITTMANN¹, ALEXANDER KANN¹

5

6 ¹Department of forecasting models, Central Institute for Meteorology and
7 Geodynamics, Vienna, Austria

8

9

10

11 (Submitted to Geoscientific Model Development & Discussions)

12

13

14

15

16

17 ^{*}Corresponding author address: Yong Wang, Department of forecasting models,
18 Zentralanstalt für Meteorologie und Geodynamik, Hohe Warte 38, A-1190 Vienna,
19 Austria.

20 E-Mail: yong.wang@zamg.ac.at

21

22

23

24

25

ABSTRACT

26

27 The 2.5 km convection-permitting (CP) ensemble AROME-EPS (**A**pplications of
28 **R**esearch to **O**perations at **M**esoscale – **E**nsemble **P**rediction **S**ystem) is evaluated
29 by comparison with the regional 11 km ensemble ALADIN-LAEF (**A**ire **L**imitée
30 **A**daption dynamique **D**éveloppement **I**nter**N**ational - **L**imited **A**rea **E**nsemble
31 **F**orecasting) to show whether a benefit is provided by a CP EPS. The evaluation
32 focuses on the abilities of the ensembles to quantitatively predict precipitation during
33 a 3-month convective summer period over areas consisting of mountains and
34 lowlands. The statistical verification uses surface observations and 1 km x 1 km
35 precipitation analyses, and the verification scores involve state-of-the-art statistical
36 measures for deterministic and probabilistic forecasts as well as novel spatial
37 verification methods. The results show that the convection-permitting ensemble with
38 higher resolution AROME-EPS outperforms its mesoscale counterpart ALADIN-LAEF
39 for precipitation forecasts. The positive impact is larger for the mountainous areas
40 than for the lowlands. In particular, the diurnal precipitation cycle is improved in
41 AROME-EPS, which leads to a significant improvement of scores at the concerned
42 times of day (up to approximately one third of the scored verification measure).
43 Moreover, there are advantages for higher precipitation thresholds at small spatial
44 scales, which is due to the improved simulation of the spatial structure of
45 precipitation.

46

47

48 **1. Introduction**

49 The prediction of deep convection in mountainous terrain is known to be one of the
50 greatest challenges in atmospheric modeling. The initiation and development of deep
51 convection is dependent on small-scale orographic structures and related processes,
52 which cannot be easily described by atmospheric models (Wulfmeyer et al. 2011,
53 Barthlott et al. 2011, Weckwerth et al. 2014). Nevertheless, the estimation of the
54 location, duration and intensity of precipitation events is important as alpine areas are
55 more exposed to natural hazards connected with heavy precipitation (landslides and
56 flooding) than flat land (e.g. Rotach et al. 2009, Haiden et al. 2014).

57 Models with deep convection-parameterization perform poorly in simulating heavy
58 and highly localized precipitation, especially those with a grid-spacing larger than 10
59 km (Weusthoff et al. 2010). One source of errors is that the applied convection
60 schemes act independently in individual model grid columns. As a consequence,
61 convectively generated cold-pools that drive convective system propagation cannot
62 be properly simulated, resulting in simulated system movement that is too slow. In
63 weak synoptic forcing, for example, organized MCSs are particularly challenging for
64 convection-parameterizing models (Clark et al. 2007; Liu et al. 2006). Another
65 drawback is that the inadequate descriptions of buoyancy and updrafts in a
66 convection-parameterizing model often cause convection to initiate too early. This
67 premature initiation of convection often results in timing and location errors as well as

68 difficulties to simulate the diurnal cycle of rainfall (Clark et al. 2007). Detailed
69 discussion on the convection initiation in a convection-parameterizing model can be
70 found in Davis et al. (2003) and Bukovsky et al. (2006).

71 A solution for this kind of forecasting problem is offered by a new generation of
72 numerical weather prediction (NWP) models, which have been developed during the
73 last decade. Convection-permitting models with horizontal grid-spacings of
74 approximately 2 km – 3 km offer new possibilities for estimating local impacts. The
75 term *convection permitting* as used in this article (*CP* hereafter) means that a deep
76 convection parameterization is not used in the model. It is assumed that the
77 horizontal resolution around 2-3 km is sufficient to depict the bulk properties of
78 precipitating convective cells, but not to truly resolve the processes within
79 precipitating convective cells such as turbulence and entrainment (Bryan et al. 2003).
80 This is in accordance with Weisman et al. (1997) who suggested setting the upper
81 limit for the range of *convection allowing* resolutions at 4 km.

82 Despite the higher resolution and explicit simulation of deep convection, the exact
83 prediction of location, intensity and spatio-temporal extent of deep convection is still
84 difficult. Recently, probabilistic approaches using convection-permitting ensembles
85 have proven valuable, since they provide direct information on forecast uncertainty,
86 which is often quite large for deep convection. An ensemble usually consists of a
87 number of model runs, which differ in their initial and boundary conditions and/or
88 model configurations. In order to produce a reliable probabilistic forecast, the
89 individual ensemble member forecasts should be equally likely to occur and cover
90 the range of future states. Following Clark et al. (2011), the ideal number of

91 ensemble members is dependent on the point of *diminishing returns*, i.e. the
92 ensemble size where no new information can be expected by additional members.

93 In the recent years several CP EPSs have been developed and some experiences
94 with them have already been made. To name but a few, there are the COSMO-DE-
95 EPS (**C**onsortium for **S**mall-scale **M**odeling – EPS, Gebhardt et al. 2011; Peralta et
96 al. 2012; Bouallègue et al. 2013; Kühnlein et al. 2014) at the Deutscher Wetterdienst
97 (DWD), the CP version of UK Met Office’s MOGREPS (**M**et **O**ffice **G**lobal and
98 **R**egional **E**nsemble **P**rediction **S**ystem, Bowler et al. 2008; Caron 2013; Hanley et al.
99 2013; Tennant 2015), a Storm Scale Ensemble Forecast (SSEF) run by the Center of
100 Analysis and Prediction of Storms (CAPS) at the University of Oklahoma (Xue et al.
101 2007, 2009; Clark et al. 2011; Schumacher et al. 2013 and Schumacher and Clark
102 2014), WRF based CP ensemble at NCAR (Schwartz et al. 2014) and AROME-EPS
103 (e.g. Vié et al. 2012; Bouttier et al. 2012) developed at Météo-France. A common
104 feature of all of these EPSs is that their horizontal mesh size is equal to or less than
105 4 km, but mostly between 2 km and 3 km.

106 The EPSs mentioned above differ regarding their number of ensemble members and
107 their perturbation strategies and post-processing. Some of them apply an ensemble
108 data assimilation (EDA) approach for perturbing the initial conditions (ICs) (Vié et al.
109 2012; Caron 2013; Schumacher and Clark 2014; Schwartz et al. 2014). The applied
110 model perturbation methods range from a multi-parameter approach (Gebhardt et al.
111 2011) to a stochastic physics scheme (Bouttier et al. 2012; Romine et al. 2014) and
112 to using different dynamical cores (Schumacher et al. 2013). In order to increase
113 ensemble size and to improve the representation of the ensemble distribution some

114 systems also apply the neighborhood method and/or lagged ensemble concepts
115 (Bouallègue et al. 2013). While the neighborhood method is based on ensemble
116 probabilities derived from grid points of a defined environment (Theis et al. 2005,
117 Schwartz et al. 2010), the lagged ensemble approach uses forecasts of successive
118 ensemble runs (Bouallègue et al. 2013).

119 A number of evaluative studies concerned with these CP-EPSs have been
120 conducted. They mainly focus on the investigation of the impact of CP ensemble
121 configurations, for example, the generation of IC perturbation, representation of the
122 model error, uncertainties from the lateral boundary conditions (LBCs), ensemble
123 size, and spatial scale (Kong et al. 2006; Clark et al. 2009; Clark et al. 2011; Vié et
124 al. 2012; Bouttier et al. 2012; Bouallègue et al. 2013; Kühnlein et al. 2014; Schwartz
125 et al. 2014; Schumacher and Clark 2014; Romine et al. 2014; Tennant 2015). There
126 are few comprehensive studies on the evaluation of CP EPS, in particular, in
127 comparison with the mesoscale regional EPS. Clark et al. (2009) compared a 5-
128 member 4 km grid-spacing convection allowing ensemble with a 15-member 20 km
129 grid-spacing regional ensemble. Their case studies reveal that the convection
130 allowing ensemble generally provides more accurate precipitation forecasts than the
131 coarser resolution regional EPS. These results are consistent with those found by
132 Taraphdar et al. (2014) who showed the superior forecast quality of deterministic
133 high-resolution forecasts of tropical cyclone tracks and the accompanying rainfall
134 intensities.

135 In this paper, we will evaluate the performance of a 16-member 2.5 km grid-spacing
136 convection permitting EPS by comparing it with its driving ~~16-~~member and 11 km

137 grid-spacing mesoscale regional ensemble. Focus will be on the capabilities of the
138 CP ensemble to quantitatively predict precipitation during a convective summer
139 period over an area consisting of mountains and lowlands. Of interest here is the
140 Alpine region, since the impacts of the mountainous terrain, such as windward/lee
141 effects, the differential heating of valley and mountain slopes can cause large
142 inaccuracies in forecasting convective precipitation and pose a challenge for
143 numerical models and their physical parameterizations (Richard et al. 2007;
144 Wulfmeyer et al. 2008, Bauer et al. 2011, Wulfmeyer et al. 2011). Therefore, an
145 evaluation study is designed and conducted for a typical convective season (3
146 months, May – August 2011), i.e. a period, which is long enough to make at least
147 basic statements about the significance of results. Naturally, this period length is not
148 sufficient to enable statistically reliable statements on real hazardous events, such as
149 landslides and flashfloods. However, the investigations can be regarded as a first
150 step towards this aim. The CP ensemble, which is evaluated in this paper, is a
151 version of AROME-EPS, developed at the Central Institute for Meteorology and
152 Geodynamics in Austria (ZAMG). It is compared with its coarser driving regional EPS
153 ALADIN-LAEF (Wang et al. 2011). The following questions are raised:

- 154 • Can a convection permitting EPS provide an advantage over its coarser,
155 driving regional EPS in complex terrain?
- 156 • Is there any difference of the performance for the compared EPSs between
157 lowlands and mountainous areas?

- 158 • How well can CP EPS and lower resolution regional EPS simulate the diurnal
159 cycle of precipitation? Is the onset and development of convective
160 precipitation realistic?
- 161 • Does a significant difference in performance for different weather regimes
162 (i.e. days with weak and strong synoptic forcing) exist?

163 A verification study is designed and conducted to answer these questions and to
164 establish whether AROME-EPS can outperform ALADIN-LAEF, a regional
165 mesoscale ensemble with deep convection parameterization on a coarser grid. Wang
166 et al. (2012) demonstrated the added value of ALADIN-LAEF as a regional
167 mesoscale EPS to the global ECMWF-EPS (European Centre for Medium-Range
168 Weather Forecasts). Hence, the present study extends this research by addressing
169 the step between regional mesoscale and CP ensembles.

170 For the present paper, AROME-EPS is coupled to the 16 perturbed ALADIN-LAEF
171 members. This is done to take advantage of the simulation of uncertainties used in
172 ALADIN-LAEF. This uncertainty information is subsequently transferred to finer
173 scales via the dynamical downscaling of the ALADIN-LAEF forecasts by AROME.
174 This means that, both IC perturbations and LBC perturbations are provided from the
175 driving model and are, thus, consistent. No further IC perturbations and model
176 perturbations are applied. Generally, the set-up is kept as simple as possible to point
177 out the pure effects of the downscaling: AROME-EPS is directly coupled to a daily
178 ALADIN-LAEF run initiated at 00 UTC. There is no time lag between the ALADIN-
179 LAEF and the AROME-EPS simulations and the forecasts are evaluated for the first
180 30h of the model runs, hence for a whole day and the subsequent night each.

181 The benefits of AROME-EPS compared to ALADIN-LAEF are revealed in the
182 framework of a comparative verification study. Although the focus of the verification
183 study is on the onset and development of precipitation, the performance of other
184 surface weather parameters are considered. The verification methods are selected in
185 such a way that the overall performance, in a deterministic and probabilistic manner,
186 and the abilities of the ensembles to reproduce spatial structures, can be
187 investigated. Hence, ensemble-related scores are combined with spatial verification
188 methods.

189 More detailed characteristics of the compared models are described in Section 2
190 along with the verification data. The methods chosen for the evaluation of the two
191 ensembles are described in Section 3. Section 4 comprises the verification results
192 and Section 5 the summary and concluding remarks.

193 **2. Ensemble systems and data**

194 *a. The regional ensemble ALADIN-LAEF*

195 ALADIN-LAEF is the operational regional ensemble system of ZAMG and runs at
196 ECMWF (Wang et al. 2010, 2011). It is based on the hydrostatic spectral limited area
197 model ALADIN (Wang et al. 2009). ALADIN-LAEF has 16 members and is coupled to
198 ECMWF-EPS (Weidle et al. 2013) with a horizontal grid-spacing of 11 km. In
199 operational mode it ~~and~~ runs two times per day at 0000 and 1200 UTC and provides
200 probabilistic forecasts on a forecast range up to 3 days ahead, i.e. 72 h. In this study,
201 however, evaluation is confined to the run at 00 UTC and a forecast range of 30 h

202 | ~~ahead only. This is done in order to investigate the onset and development of~~
203 | ~~convection in its diurnal cycle.~~

204 | ~~with a horizontal grid spacing of 11 km.~~The 16 members of ALADIN-LAEF are not
205 | sufficient to represent the atmospheric state probability density function (PDF).
206 | However, Schwartz et al. (2014) have shown that similar verification scores can be
207 | obtained from a 50-member ensemble and subsets of 20-30 members. Hence, we
208 | can expect, at least, reasonable results from verification based on a 16-member
209 | ensemble.

210 | ~~The goal of ALADIN-LAEF is to provide probabilistic forecasts on a forecast range up~~
211 | ~~to 3 days ahead, i.e. 72 h, although only 30 h are used in this study for the~~
212 | ~~comparison with AROME-EPS.~~The ALADIN-LAEF domain (Figure 1) covers the

213 | whole European continent, Iceland, the whole Mediterranean Sea, Black Sea,
214 | Caspian Sea and adjacent countries. The eastern margins reach the Ural Mountains
215 | and parts of Siberia. To deal with the atmospheric initial condition perturbation
216 | ALADIN-LAEF applies a breeding-blending method for generating the IC
217 | perturbations for the upper levels. It uses large-scale perturbations from the driving
218 | global-ECMWF-EPS combined with small-scale perturbations from the ALADIN-
219 | breeding vectors (Toth and Kalnay 1993). The blending method (Wang et al. 2014)
220 | ensures that inconsistencies between small and large-scale perturbations are
221 | avoided. Therefore a digital filter is applied on the low spectral truncations of both the
222 | breeding-vectors and the fields from the global model. Afterwards the filtered
223 | breeding vectors on the full spectral resolution are subtracted from the original ones

224 and added by the filtered global fields resulting in initial perturbations that are
225 consistent with the regional EPS itself as well as with the driving global EPS.

226 To consider uncertainties arising from the initial surface conditions in ALADIN-LAEF,
227 a surface data assimilation scheme based on optimum interpolation (CANARI - Code
228 for the Analysis Necessary for Arpege for its Rejects and its Initialization, Taillefer
229 2002) is implemented using randomly perturbed observations. To account for
230 uncertainties in the model itself, a multi-physics approach is implemented in ALADIN-
231 LAEF. The perturbed members use different model configurations with several
232 combinations and tunings of schemes and parameterizations available in the ALADIN
233 physics package. The main emphasis is put on the variation and tunings of the
234 following schemes and parameterizations: The diagnostic convection scheme as
235 described in Bougeault (1985); the prognostic deep convection scheme 3MT
236 (modular multi-scale **M**icrophysics and **T**ransport scheme, Gerard et al. 2009), and
237 the connected microphysics scheme described in Geleyn et al. 2008 and Gerard et
238 al. (2009); the radiation scheme based on Ritter and Geleyn (1992) or alternatively
239 the scheme described in Mlawer (1997) and Morcrette (1991); the pseudo prognostic
240 TKE (**T**urbulent **K**inetic **E**nergy) scheme described in Vana et al. (2008). Further
241 details can be found in (Wang et al. 2010).

242 *b. The convection permitting ensemble AROME-EPS*

243 The model core of AROME-EPS is the non-hydrostatic spectral limited area model
244 AROME (Seity et al. 2011), which is especially designed to run at very high
245 resolutions with a grid-spacing of 2.5 km or lower. Deep convection is treated
246 explicitly, while shallow convection is parameterized with a mass flux approach

247 (Pergaud et al. 2009). The single moment bulk microphysics scheme ICE3 for mixed-
248 phase cloud parameterization (Pinty and Jabouille 1998) can handle mixing ratios of
249 five prognostic hydrometeor classes: cloud water, cloud ice, rain, snow and graupel
250 and also simulates complex interactions between them. AROME by default uses a
251 three-layer soil model SURFEX (Surface Externalisé) with the effects of sea and
252 urban areas parameterized using a tile approach (Masson et al. 2000).

253 At ZAMG a deterministic version of AROME with 2.5 km grid-spacing has been
254 operational since January 2014 running every 3 hours up to a lead-time of 48 hours.
255 The domain for the model integration encompasses the Alpine region (Figure 1).
256 Table 1 summarizes the most important model characteristics of ALADIN-LAEF and
257 AROME-EPS.

258 To run AROME-EPS, the same version of AROME with the same resolution is
259 initialized by a dynamical downscaling of ALADIN-LAEF and coupled to the 16
260 members of ALADIN-LAEF. The ensemble runs with a forecast range of 30 h are
261 initiated at 00 UTC each day, i.e. at the same time as ALADIN-LAEF. There is no A
262 time lag ~~is not~~ considered, as the pure impact of enhanced resolution and the
263 convection-permitting configuration shall be investigated. Apart from the
264 perturbations of initial conditions and lateral boundary conditions, no further
265 perturbations (such as e.g. multi-physics parameterizations as in ALADIN-LAEF) are
266 induced in the model integration. This comparatively simple configuration is used for
267 several reasons: First, AROME-EPS has been set up quite recently at ZAMG and is
268 still at an early stage of development. Secondly, the development of physics
269 perturbations in AROME-EPS will rather go towards a stochastic physics scheme or

270 a combined stochastic/multi-physics scheme than towards pure multi-physics as
271 currently used in ALADIN-LAEF. And thirdly, the aim of this study is to test the
272 possible advantage of a CP EPS compared to the operational system of ALADIN-
273 LAEF.

274 *c. Verification data*

275 Station observations are used for the evaluation of ALADIN-LAEF and AROME-EPS
276 surface weather variables. Figure 2 shows the 517 surface stations in the AROME
277 domain, providing observations at 6-hourly intervals for 2 m temperature, 2 m
278 humidity, 10 m wind speed and mean sea level pressure. The upper level verification
279 is achieved using ECMWF analyses reference data at four pressure levels: 925 hPa,
280 850 hPa, 700 hPa, and 500 hPa, which are adapted to the model resolutions of both
281 AROME-EPS and ALADIN-LAEF.

282 The evaluation of precipitation forecasts is performed using the very high-resolution
283 precipitation analyses of the ZAMG nowcasting system INCA (Integrated Nowcasting
284 through Comprehensive Analyses; Haiden et al. 2011). This is necessary as the
285 average station distance of precipitation observations is too large to resolve the fine
286 spatial structures of precipitation events. The advantage of the INCA analyses is that
287 they use additional observations and are provided on a regular grid. Based on this
288 gridded data, it is possible to apply enhanced verification methods on precipitation
289 fields, which cannot be computed on a point-to-point basis.

290 The INCA system, developed at ZAMG, operates on a horizontal resolution of 1 km x
291 1 km. INCA blends data from automatic weather stations, remote sensing data

292 (radar, satellite), forecast fields of numerical weather prediction (NWP) models, and
293 high-resolution topographic data (Haiden et al. 2011). It provides hourly 3-D fields of
294 temperature, humidity, wind, and 2-D fields of cloudiness, precipitation rate and
295 precipitation type with an update frequency of 15 minutes to 1 hour. The precipitation
296 analyses are provided for different accumulation periods. In the present study, the
297 one-hour accumulated INCA precipitation analyses are used as a reference for the
298 spatial verification of EPS forecasts. For these analyses, precipitation measurements
299 from surface stations and radar data are accumulated to one-hour sums and
300 algorithmically merged. Prior to the analysis procedure, the data are quality
301 controlled and climatologically scaled (Haiden et al. 2011). In this way the higher
302 quantitative accuracy of the station data and the better spatial coverage of the radar
303 data are utilized. The resulting analysis reproduces the observed values at the
304 station locations while preserving the spatial structure provided by the radar data.
305 The analysis error, which is computed from classical cross-validation, varies from
306 case to case and depends on precipitation type, e.g. large-scale or convective, and
307 on the accumulation period. The magnitude of analysis errors of grid point values can
308 be quite large, but areal mean values are significantly more reliable (Haiden et al.
309 2011)

310 Amending the rain gauge - radar combination, the scheme includes elevation effects
311 on precipitation using an intensity-dependent parameterization (Haiden and Pistotnik
312 2009). A NWP model first guess is not required in the precipitation analysis, thus
313 such analyses are ideally suited as an independent reference to validate NWP
314 models.

315 Forecast verifications are performed at the observation locations for surface variables
316 as 2 m temperature and humidity, 10 m wind speed and mean sea level pressure,
317 and on the INCA grid for precipitation. The model forecasts are interpolated bi-
318 linearly to the station locations and INCA analysis grid points, respectively. Further, a
319 height correction scheme is applied on 2 m temperature values based on
320 atmospheric standard conditions. In doing so, the same number of
321 forecast/observations pairs is available for the verification of each of the EPS models.
322 This supports the comparability of the verification results.

323 **3. Verification strategy**

324 AROME-EPS and ALADIN-LAEF are evaluated over a 3-month summer period from
325 15 May, 2011 – 15 August, 2011, which represents a typical convective summer
326 season in Central Europe.

327 Precipitation is one of the parameters for which the biggest improvement is expected
328 from the convection-permitting models. Therefore, the evaluation of the ensembles
329 focuses on the representation of the spatio-temporal structure of precipitation events
330 in the forecasts. Nevertheless, the preconditions for the development and onset of
331 precipitation are also considered. For this reason other forecast parameters, such as
332 temperature, humidity, wind speed, air pressure and geopotential height are also
333 verified.

334 Precipitation forecasts are evaluated in both deterministic and probabilistic ways. The
335 deterministic approach is directed towards predicting the correct precipitation
336 amounts and the spatial distribution of the data. Probabilistic evaluation tests the

337 capability of the ensembles to predict a pre-defined event with the probability, which
338 corresponds to its relative frequency, i.e. to produce a reliable PDF for the
339 occurrence of the event. The events can be defined as, e.g., precipitation amounts
340 exceeding a certain threshold. In this study, thresholds of 0.1 mm (threshold for the
341 prediction of *rain* or *no rain*), 0.5 mm, 1 mm, 2 mm and 5 mm are chosen for 3-hourly
342 accumulated precipitation amounts. These thresholds appear low, especially when
343 taking into account convective precipitation events. However, the thresholds are
344 selected according to the frequency of occurrence of the precipitation values in the
345 individual grid cells of the 1 km x 1 km verification grid. They ensure that a sufficient
346 number of observed events are available for evaluation over the 3-month test period.
347 The two ways of deterministic and probabilistic evaluation reflect the main options for
348 the efficient use of ensemble forecasts: First, as a conservative prediction of
349 ensemble mean or median or, second, as a tool to estimate the uncertainty of the
350 forecast and the probability of extreme values via the ensemble spread and PDF
351 (e.g. Zhu et al. 2002).

352 | ~~A number of t~~Traditional point-to-point verification scores (see e.g. Wilks 2006) ~~in~~
353 | ~~Table 2~~ are computed for all evaluated parameters. In addition, significance tests for
354 | these scores are performed. Confidence intervals of the verification scores are
355 | estimated by a bootstrapping algorithm (Davison and Hinkley 1997; Joliffe 2007;
356 | Ferro 2007) and confidence intervals of 90%. The bootstrapping method uses 5000
357 | random samples with a block length of eight.

358 | In order to present the results concisely, ~~only~~ three scores have been selected ~~from~~
359 | ~~Table 2~~ to describe the differences in forecast performance between AROME-EPS

360 and ALADIN-LAEF: Bias (Eq. 1), Brier Score (BS, Brier 1950, Eq. 2) and Continuous
361 Ranked Probability Score (CRPS, Hersbach 2000; Gneiting and Raftery 2007; Eq. 3).

362 The Bias simply measures the mean deviation between the analyzed values (a) and
363 the forecast values, in our case the ensemble means (\bar{f}), at n grid points i . Both,
364 positive as well as negative signs are possible. A perfect forecast has a bias of zero.

365 (1)
$$Bias = \frac{1}{n} \sum_{i=1}^n (\bar{f}_i - a_i)$$

366 Like the Bias also BS is a measure for the accuracy of the forecasts, however, in
367 probability space. It is the mean squared difference between the forecast probability
368 p ($p \in [0;1]$, e.g. derived from the distribution of ensemble members) for a pre-
369 defined event (e.g. the exceeding of a threshold) and the analyzed truth x ($x \in \{0,1\}$)
370). The minimal value of zero is achieved for a perfect forecast, and the maximum
371 value is one for the worst possible forecast.

372 (2)
$$BS = \frac{1}{n} \sum_{i=1}^n (p_i - x_i)^2$$

373 CRPS is related to BS insofar, as it can be expressed as the integral of BS for all
374 possible thresholds of the meteorological parameter ξ (Hersbach 2000). The value
375 for an ideal forecast of CRPS is zero as for BS.

376 (3)
$$CRPS_i = \int_{-\infty}^{\infty} [P_i(\xi) - P_i(\xi_a)]^2 d\xi$$

377 The continuous ranked probability score compares the cumulative distributions $P_i(\xi)$
378 (Eq. 4) and $P_i(\xi_a)$ (Eq. 5) of the forecast and the analyzed values at each grid point i
379 .

380 (4)
$$P_i(\xi) = \int_{-\infty}^{\xi} p_i(y) dy$$

381 (5)
$$P_i(\xi_a) = H(\xi - \xi_a)$$

382 $H(\xi)$ is the so-called Heaviside-function (Eq. 6), which only takes the values 0 and 1.

383 (6)
$$H(\xi) = \begin{cases} 0 & \text{for } \xi < 0 \\ 1 & \text{for } \xi \geq 0 \end{cases}$$

384 | In addition to those traditional statistical scores ~~in Table 2~~, precipitation forecasts are
385 verified by spatial verification methods, which not only consider the exact match of
386 forecast and verification values at individual points, but take into account the
387 matching of forecasts and observations in terms of objects or spatial scales (Casati
388 et al. 2008, Ahijevych et al. 2009, Gilleland et al. 2010). This is necessary as
389 precipitation fields exhibit high spatial variability and discontinuity. Small deviations in
390 space and time between forecast and verification data can lead to large errors in
391 traditional point to point verification scores, which is also known as the *double*
392 *penalty* problem (Nurmi 2003).

393 *a. Spatial verification methods*

394 The selected spatial verification methods are the so-called SAL method (Structure-
395 Amplitude-Location method, Wernli et al. 2008) and the Fractions Skill Score
396 (Roberts and Lean 2008).

397 SAL determines the forecast performance in terms of structure (S), amplitude (A) and
398 location (L). The method is object based. Precipitation objects in forecast and
399 verification fields are contiguous areas of grid-points exceeding a certain precipitation
400 threshold.

401 (7)
$$A = \frac{\bar{R}_f - \bar{R}_a}{0.5[\bar{R}_f + \bar{R}_a]}$$

402 The amplitude score (Eq. 7) defines whether the integrated precipitation amount \bar{R} of
403 the field is underestimated ($A < 0$) or overestimated ($A > 0$). Subscripts, f and a ,
404 denote forecast and analyzed fields, respectively.

405 The location score measures the agreement of the centers of mass in the analyzed
406 and predicted precipitation fields together with the averaged distance between the
407 center of mass and the individual objects. It is actually the sum of two components $L =$
408 $L1 + L2$ where both values are in the range $[0, 1]$. The first part $L1$

409 (8)
$$L1 = \frac{|x(R_f) - x(R_a)|}{d_{\max}}$$
,

410 is a measure of the distance between the mass centers x of the analyzed (R_a) and
411 the predicted precipitation fields (R_f). d_{\max} is the longest possible distance in the
412 domain.

413 As an identical mass center position does not necessarily mean that the forecast is
 414 perfect, the second component L2 (Eq. 9) is introduced:

$$415 \quad (9) \quad L2 = 2 \frac{|r(R_f) - r(R_a)|}{d_{\max}}$$

416 L2 takes into account the distance r (Eq. 10) between the mass center of each
 417 individual object R_n and the overall mass center and compared between the
 418 observed and simulated precipitation field:

$$419 \quad (10) \quad r = \frac{\sum_{n=1}^M R_n |x - x_n|}{\sum_{n=1}^M R_n}$$

420 The L component has a range [0, 2] with $L=0$ indicating a perfect forecast.

421 The structure score S

$$422 \quad (11) \quad S = \frac{V(R_f) - V(R_a)}{0.5[V(R_f) + V(R_a)]}$$

423 compares the weighted sums of the precipitation volumes $V(R)$

$$424 \quad (12) \quad V(R) = \frac{\sum_{n=1}^M R_n V_n}{\sum_{n=1}^M R_n}$$

425 of the precipitation objects, where the $V_n = R_n / R_{\max}$ describe precipitation sums
 426 scaled by their maxima. If $S < 0$, forecast objects are too small and too peaked. In
 427 contrast, $S > 0$ indicates that the objects are too large and too flat.

428 The fractions skill score (FSS)

429 (13)
$$FSS(n) = 1 - \frac{MSE(n)}{MSE(n)_{ref}}$$

430 evaluates the forecasts on different spatial scales. The scales are defined via
 431 neighborhoods, i.e. square boxes of length n grid spaces surrounding a selected grid
 432 point. The score compares the fractions of rain coverage of forecast and analysis in
 433 the neighborhoods. Depending on the precipitation event, small disparities of the
 434 coverage may lead to large forecast errors on fine scales, but to a better rating on a
 435 coarser scale. The aim of FSS is to identify scales for which the evaluated model can
 436 provide useful forecasts.

437 FSS is computed by assigning the grid points binary values 0 and 1 in each of the
 438 neighborhoods with subscripts (i,j) , according to a selected precipitation threshold.
 439 From these binary fields, the fraction of the points with value 1 are computed for
 440 analyses and forecasts as $A_{(n)i,j}$ and $F_{(n)i,j}$, respectively.

441 At each such defined scale n , the mean squared error (MSE):

442 (14)
$$MSE_{(n)} = \frac{1}{N_x N_y} \sum_{i=1}^{N_x} \sum_{j=1}^{N_y} [A_{(n)i,j} - F_{(n)i,j}]^2$$

443 is computed for the whole field of fractions and related to a reference (MSE_{ref})

444

445 (15)
$$MSE_{(n)ref} = \frac{1}{N_x N_y} \left[\sum_{i=1}^{N_x} \sum_{j=1}^{N_y} A_{(n)i,j}^2 + \sum_{i=1}^{N_x} \sum_{j=1}^{N_y} F_{(n)i,j}^2 \right]$$

446 MSE_{ref} is the largest possible MSE, which can be obtained from the underlying field.
447 The skill score summarizes the performance in the whole field and ranges from 0
448 (complete mismatch) to 1 (perfect match).

449 *b. Subdomains for precipitation verification*

450 Verification is done for the whole domain *Austria*. To account for the different
451 topographic characteristics in the verification domain, two sub-domains are chosen
452 (Figure 3). They comprise mountainous area (region *West*) as well as region with flat
453 terrain (region *Northeast*). Due to the location of the Alps in Austria and the prevailing
454 flow directions around the Alps, each of the subdomains has its own climatological
455 properties, which is also visible in the precipitation characteristics.

456 *c. Temporal stratification*

457 In order to investigate the influence of different weather regimes, the 92 days of the
458 test period are classified into three bins according to the synoptic situation, *strong*
459 *synoptic forcing*, *weak synoptic forcing*, and *dry*. Days are classified as *dry* (5 days) if
460 the areal mean of the daily precipitation sum is below 0.05 mm. All other days, i.e. 87
461 days on which rains was reported, are assigned to the bins of *weak* (23 days) or
462 *strong synoptic forcing* (64 days). For the classification, a method described by Done
463 et al. (2006) and successfully applied by Kühnlein et al. (2014) is used which is
464 based on the temporal variability of CAPE (**C**onvective **A**vailable **P**otential **E**nergy) as
465 a measure of atmospheric instability. According to Done et al. (2006), the approach

466 helps to distinguish between days on which convection is predominantly at
467 *equilibrium* or at *non-equilibrium*. This means that the destabilization of the
468 atmosphere by large-scale synoptic forcing is balanced or un-balanced, respectively,
469 by the stabilization through convection. The idea is that this balance or imbalance is
470 related to the timescale in which CAPE is built up by large-scale processes and
471 consumed by convection. On days with *weak synoptic forcing* the consumption of
472 CAPE is related to the diurnal cycle or to local triggering rather than to prevalent
473 large-scale processes. In these cases the convective timescale is long and CAPE is
474 often not fully consumed by convection. In situations where CAPE is realized much
475 faster by large-scale processes, i.e. in situations of *strong synoptic forcing*,
476 convection is in equilibrium. In our study the *convective adjustment time-scale* t_c

477 (16)
$$t_c = \text{CAPE} \frac{d(\text{CAPE})}{dt}$$

478 is calculated hourly from AROME-EPS CAPE forecasts using $\Delta t = 1h$. Following the
479 suggestion of Done et al. (2006) a specific day is assigned to *weak synoptic forcing* if
480 the areal mean of t_c exceeds a threshold of 6 h at least once a day by at least three
481 ensemble members. In order to test the method of Done et al. (2006) we compared
482 the classification with alternative approaches, such as the temporal change of mid-
483 tropospheric vorticity and convection related to patterns in 500 hPa geopotential
484 using archived ECMWF forecast and ERA-Interim re-analyses. The results were
485 comparable to those of the equilibrium method.

486 **4. Results**

487 In the following we present the evaluation of AROME-EPS and ALADIN-LAEF over a
488 three-month summer period. The focus is on the performance of near surface
489 parameters, in particular the precipitation forecast, which is of most interest to the
490 users of convection permitting and regional EPSs.

491 *a. Evaluation of forecasts of temperature, wind and humidity*

492 The forecast performance of surface parameters (2 m temperature and humidity, 10
493 m wind speed and mean sea level pressure MSLP) and upper level parameters
494 (temperature, humidity, wind speed and geopotential height) of AROME-EPS and
495 ALADIN-LAEF are verified in this study, which form the background of the evaluation
496 of precipitation.

497 A large number of verification metrics (~~Table 2~~) have been calculated for those near
498 surface and upper air parameters. In general there is no clear advantage either for
499 ALADIN-LAEF or for AROME-EPS. Exceptions from this statement are solely
500 constituted by biases in the forecasts, which are particularly found on the surface
501 level. They form the most eminent differences in the performances of the EPSs: If the
502 bias is low, the models provide good performance also for other scores.

503 For the surface level, we also found more results on a high level of significance (i.e.
504 90%). The verification results of the upper levels are less significant than for the
505 surface and performance is more ambivalent. We used a large number of
506 observations for both surface (station observations) and upper levels (ECMWF grid
507 values). Hence, the lower significance of the results for the upper levels can be
508 explained by the model set-up rather than by the verification data. Near surface and

Formatiert: Schriftart: 12 Pt.

Formatiert: Schriftart: 12 Pt.

509 on lower levels AROME-EPS can add more information to the model simulation
510 compared to ALADIN-LAEF than on higher levels. This is due to the SURFEX soil
511 scheme and the interaction between a refined representation of orography and the
512 model physics schemes and dynamics. On the higher levels, however, there is less
513 influence of the orography and the simulation resembles more the driving model. For
514 this reasonTherefore, surface results have been selected to highlight the main
515 findings in the following.

Formatiert: Schriftart: 12 Pt.

516 Figure 4 compares the bias and Continuous Ranked Probability Score (CRPS, see
517 Wilks 2006 for details) for 2 m relative humidity, 2 m temperature and 10 m wind
518 speed. CRPS compares the forecast PDF to the observed values of occurrence and
519 non-occurrence, respectively. CRPS is sensitive to the difference between the
520 forecast probabilities to observed values. The lower the difference, the better the
521 forecast is rated. Hence, the value of CRPS of a perfect forecast is zero. Due to its
522 formulation, signals of CRPS are also reflected by many other scores, in particular
523 those which are sensitive to deviations between the distributions of forecasts and
524 observations. Thus, CRPS is useful for representing the results of this study
525 exemplarily. It also shows the impact of biased forecasts.

526 Biases of 2 m relative humidity in Fig. 4a show noticeable diurnal variations. During
527 the night and early morning, AROME-EPS is too dry, whereas ALADIN-LAEF is too
528 moist during the day (1200 UTC and 1800 UTC). The diurnal variations of the
529 differences between AROME-EPS and ALADIN-LAEF are also reflected in CRPS in
530 Figure 4b. During the night, AROME-EPS and ALADIN-LAEF are at the same level,
531 but for the day hours AROME-EPS shows better results. For 2 m relative humidity,

532 most verification results are significant at a level of 90%. This is also true for the
533 differences in forecast performance during the day hours. Results for 2 m
534 temperature in Figures 4c and 4d show an improvement for most of the used scores
535 at a significance level of 90% for AROME-EPS. This result is partially due to a large
536 bias of ALADIN-LAEF temperatures. In contrast, there exist fewer deviations
537 between the ensembles for wind speed (Figures 4e and 4f) and MSLP (not shown).
538 However, these results have only a low level of significance.

539 *b. Evaluation of precipitation forecasts*

540 Precipitation is evaluated by 3-hourly INCA analyses on a regular 1 km x 1 km grid. A
541 first insight of the strengths and weaknesses of the ensembles in forecasting
542 precipitation is offered by a comparison of the daily variability of precipitation
543 intensities. Figure 5 compares the 3-hourly precipitation sums of INCA and both EPS
544 models for different regional domains and for days with strong (left panels) and weak
545 (right panels) synoptic forcing.

546 Errors occur in terms of over- and underestimation of the maximum intensity and in
547 terms of time shifts. The daily maximum of 3 h-precipitation is overestimated by
548 AROME-EPS for regions *West* and *Austria* and both types of synoptic forcing by
549 20%-50%. In ALADIN-LAEF, the maximum in these regions is approximately at the
550 same level as analyzed by INCA. Hence, the too moist conditions of ALADIN-LAEF
551 near the surface in Fig. 4a are not reflected in the precipitation sums. For region
552 *Northeast*, AROME-EPS correctly simulates the maximum amount of precipitation,
553 whereas ALADIN-LAEF is too low.

554 Considering the days with strong synoptic forcing in Figure 5 (left panels), the highest
555 precipitation sums are detected around 1800 UTC. AROME-EPS describes the
556 temporal maximum quite well, whereas the maximum in ALADIN-LAEF occurs too
557 early (-3 h time shift). In the case of weak synoptic forcing shown in Figure 5 (right
558 panels), the precipitation maxima are observed later than for the other cases in
559 region *West* (e.g. 2100 UTC instead of 1800 UTC). This is not reflected by the EPS
560 models, which both reach the maximum intensity of precipitation at 1500 UTC. Only
561 for region *Northeast* and weak synoptic forcing does the maximum of precipitation
562 occur too late in AROME-EPS. The characteristic that ALADIN-LAEF and AROME-
563 EPS tend to trigger moist and deep convection over complex orography too early is
564 well known (Wittmann et al. 2010). However, according to Figure 5, running a model
565 or an EPS on CP scales is beneficial for predicting the daily maximum of the
566 convective diurnal cycle, at least over mountainous terrain. With respect to the timing
567 of the maxima, AROME-EPS shows a time shift of -3 h, with ALADIN-LAEF -6 h for
568 weak synoptic forcing in regions *Austria* and *West* (panels b) and d), respectively).
569 Because of the limited framework of this study we can only speculate that this
570 behavior might be due to differences caused by the deep convection scheme in
571 ALADIN-LAEF, which is one of the reasons to cause an early onset of precipitation
572 (Bechtold et al. 2013), and respectively, the explicit simulation of deep convection in
573 AROME. Another reason, which we cannot exclude, could be that ALADIN-LAEF and
574 AROME apply different physical parameterizations. The different dynamical cores,
575 hydrostatic and non-hydrostatic, might also contribute to the differences to some
576 extent, but remain statistically less significant in respect of precipitation as shown in
577 an earlier study (Wittmann et al. 2010). Experiences concerning the pure impact of

578 different vertical resolutions on the forecast quality are few. However, it is known that
579 an increase of vertical resolution and, hence, enhanced possibilities to simulate
580 convection-related, micro-physical and boundary-layer processes, does not
581 necessarily result in an improvement of precipitation forecasts. It is rather related to
582 increased overprediction of precipitation amounts (Aligo et al. 2009).

583 A further characteristic evident in Figure 5, is that the precipitation amounts in
584 AROME-EPS develop independently of those in the driving ALADIN-LAEF members,
585 which is indicated by the ensemble spread. In ALADIN-LAEF the ensemble spread is
586 quite large for certain lead times, ranging from a larger overestimation of the
587 observed precipitation amounts to a large underestimation. This contrasts with
588 AROME-EPS, which shows a much smaller range of precipitation amounts. This
589 difference in the spread is very likely due to the large influence of the multi-physics
590 configuration in ALADIN-LAEF, compared with the single physics configuration of
591 AROME-EPS. The scores, which are discussed in the following, Brier score, SAL
592 scores and fractions skill score, demonstrate in which ways the differences in the
593 diurnal precipitation cycle have an influence on forecast quality.

594 *i. Brier score*

595 Figure 6 shows the differences of the Brier Score (BS; Brier 1950), for strong and
596 weak synoptic forcing with different precipitation thresholds. BS measures the
597 accuracy of probability forecasts, which is equivalent to the MSE for deterministic
598 forecasts. The value for perfect forecasts is zero. BS has largest values for the
599 lowest precipitation threshold (0.1 mm, upper panels), and decreases for larger
600 thresholds (2 mm, lower panels).

601 During the morning hours (+6 h, +30 h lead time), BS is low for days with weak
602 synoptic forcing. This is due to the fact, that on these days, generally stable
603 conditions prevail in the morning and precipitation probability is very low. For the
604 lower precipitation threshold, AROME-EPS shows significantly better values than
605 ALADIN-LAEF from 0900 UTC to 1500 UTC. This applies for both, days with weak
606 synoptic forcing and days with strong synoptic forcing.

607 The differences in BS between ALADIN-LAEF and AROME-EPS can, for the most
608 part, be explained by the fact that the precipitation generally starts too early in
609 ALADIN-LAEF forecasts. Additionally, the tendency of ALADIN-LAEF to forecast
610 smoother precipitation fields than AROME-EPS can be assumed as a second source
611 of errors. The smoothness leads to rather medium precipitation probabilities in large
612 areas. BS, however, accounts for sharp forecasts near zero and one (i.e. very low
613 and very high probabilities for rainfall).

614 *ii. SAL scores*

615 The variability of SAL scores with lead-time gives insight in the performance of
616 AROME-EPS and ALADIN-LAEF in terms of the structure, amplitude, and location of
617 the predicted precipitation events. Figures 7 and 8 show the SAL scores for the
618 mountainous region *West* and the lowland region *Northeast*, respectively. The
619 distributions of SAL values are sampled for the individual ensemble members and
620 classified into days with strong (panels a and b) and weak synoptic forcing (panels c
621 and d). These values differ from those based on the ensemble mean and median
622 forecasts as the averaging produces more smoothed precipitation events and, hence,
623 has an influence on the properties described by the SAL method.

624 In both geographic regions and for both types of synoptic forcing, the structure score
625 is lower for AROME-EPS than for ALADIN-LAEF, which is, inter alia, a consequence
626 of the model resolution (Wittmann et al. 2010). AROME-EPS produces precipitation
627 events, which are mostly too small and/or too peaked, whereas precipitation objects
628 in ALADIN-LAEF are too large and flat. This is particularly true for days with strong
629 synoptic forcing and for flat terrain. The structure score for ALADIN-LAEF further
630 shows a pronounced diurnal variation for region *West*, where precipitation events are
631 too large during the day (0900 – 1500 UTC), but more realistic during evening and
632 nighttime. In region *Northeast* and weak synoptic forcing, on the contrary, there is a
633 rather damped diurnal variation. This is a sign that precipitation events emerge too
634 early and grow too large over the mountains, whereas over flat land, they are too flat
635 and too widespread during the whole day. AROME-EPS generally shows better
636 agreement with the observed precipitation structures than ALADIN-LAEF during noon
637 (1200 - 1500 UTC) while objects are much too small during the rest of the day. Only
638 on days with strong synoptic forcing and over mountainous terrain does AROME-
639 EPS mostly underestimate the dimension of precipitation events. Over flat land,
640 structure scores are variable on a low level for AROME-EPS, but do not show a
641 perfect daily cycle.

642 In most instances, the amplitude component reflects the findings shown in Figure 5,
643 being more apparent for days with weak than for days with strong synoptic forcing.
644 For both EPS models, an overestimation occurs during noon over mountainous
645 terrain (region *West*, Figure 7), which is associated with the early onset of convection
646 for ALADIN-LAEF and with the overestimation of precipitation amounts in AROME-

647 EPS. In region *Northeast* (Figure 8), the agreement seems to be much better for
648 days with strong synoptic forcing than for weak synoptic forcing. However, amplitude
649 score measures the agreement in terms of the percentage share of precipitation
650 amounts. Hence, if the amounts are on a much lower level as in the case of weak
651 synoptic forcing, amplitude scores appear worse. The large amplitude errors in
652 Figures 8c and 8d are, therefore, more dependent on the time shift between
653 simulated and observed peaks of precipitation intensities than on the absolute
654 amount of maximum precipitation intensities, which are fairly well captured.

655 The location score in both regions provided by the SAL shows not as much variability
656 as the other two components. Nevertheless, an investigation of the distances of
657 observed and forecast centers of mass for the precipitation events can provide useful
658 information. Figures 9a and 9b show the mean distances for objects pertaining to
659 precipitation thresholds of 0.1 mm / 3 h and of 2 mm / 3 h for days with strong
660 synoptic forcing, respectively. In general, it can be stated that the distances get
661 shorter with increasing thresholds. This indicates that both ALADIN-LAEF and
662 AROME-EPS are more successful for more intense precipitation events. On the other
663 hand, precipitation objects with very low intensities can be either very small and
664 randomly distributed, which is difficult to predict, or very large, which is easier to
665 predict or detect.

666 For higher thresholds, Figure 9b shows that the distances have more variability with
667 time. Although distances are short for earlier hours of the forecast (and the first half
668 of the day), they increase for later forecast hours and reach a maximum at +21 h
669 (2100 UTC). This effect is much greater in ALADIN-LAEF than in AROME-EPS and it

670 is remarkable that it happens very late in the day, much later than the main peak of
671 precipitation shown in Figure 5. The reason could be that the precipitation cells are
672 captured well when they are in a mature and well developed state. Their further
673 development or collapse seems to be better simulated in AROME-EPS. This should
674 be connected to the prognostic (and explicit) treatment of the atmospheric variables
675 describing the evolution of convective activity in AROME. A convection
676 parameterization, in particular, a diagnostic convection scheme (as it is used for
677 some members of ALADIN-LAEF) has more deficiencies in simulating the life cycle of
678 convective objects properly than is the case for AROME. In addition, the non-
679 hydrostatic dynamics, higher resolution and better representation of turbulence and
680 microphysical interactions in the model physics might lead to a more realistic decay
681 of convection in AROME-EPS.

682

683 *iii.) Fractions Skill Score*

684 The fractions skill score (FSS) indicates how well the ensemble systems predict
685 precipitation at different spatial scales. The grid box widths (1 km – 21 km,
686 corresponding to areas of 1 km² – 441 km²) have been selected to investigate the
687 performance of models at very fine scales, near the resolution of the analyzed
688 observations of INCA. At these scales models have difficulties to reach the level of
689 *usefulness* (i.e. the *target skill* as defined in Roberts and Lean 2008), which can be
690 expected at larger scales. Nevertheless, it is interesting to examine how FSS values
691 change with increasing precipitation thresholds.

692 Figures 10a and 10b compare the fractional skill scores for days with strong synoptic
693 forcing and days with weak forcing. FSS values are greater (~factor 2) for strong
694 synoptic forcing than for weak synoptic forcing, since for the latter, precipitation
695 events are generally less structured which lead to the lower level of skill.

696 For all weather situations, ALADIN-LAEF shows better values for the lowest
697 thresholds of 0.1 mm and 0.5 mm. The converse result is observed for higher
698 thresholds above 2 mm. For 5 mm / 3 h ALADIN-LAEF has hardly any skill on the
699 very fine scales for days with weak synoptic forcing. This means that small, scattered
700 showers and thunderstorms, which typically occur on these days, cannot be
701 simulated well by the model with coarser model resolution. In AROME-EPS there is
702 at least a certain skill for small intense precipitation events, although it is not at a
703 level considered as reliable.

704 In the previous sections, the discussion provided an overview on the whole 3 months
705 period. In the following section, evaluations focus on a single selected day. This is
706 done in order to show the forecast behavior of the ensembles in a concrete weather
707 situation exemplarily.

708 *c. Case study*

709 A typical convective day with weak synoptic forcing is selected to show the evolution
710 of precipitation in AROME-EPS and ALADIN-LAEF in more detail. Here more
711 emphasis is put on the observation of the numbers, volumes, and distribution of the
712 precipitation objects.

713 Figure 11 illustrates the precipitation at different times of 29 April 2014 of INCA
714 analyses and the ensemble means of AROME-EPS and ALADIN-LAEF. On this day,
715 continuous light rain was reported in Austria's mountainous terrain, near the main
716 Alpine ridge during the morning hours as shown in the first row of Figure 11. At the
717 same time the lowlands in the east and north were dry. In the lowlands, precipitation
718 activities in terms of small showers started from approximately 1100 UTC in second
719 row of Figure 11. Over the course of the day the focus of precipitation was
720 increasingly shifted to the flat lands in the North, East, and Southeast of Austria as
721 well as to Slovenia and Northern Italy. The peak rain intensity was around 1500 UTC,
722 shown at 1400 UTC in third row of Figure 11. Rain in the inner alpine areas had
723 diminished. In contrast, the showers in the flat regions continued until the time of
724 sunset. Then their activity also weakened, which is visible in the bottom row of Figure
725 11.

726 Figure 12 gives the characteristics of the precipitation forecasts of ALADIN-LAEF and
727 AROME-EPS, such as the temporal evolution of the mean areal precipitation in
728 Figure 12a, the number of precipitation objects in Figure 12b, and the temporal
729 evolution of the SAL scores in Figure 12c. For the selected day, precipitation
730 amounts for the region *Austria* are slightly underestimated by the both ensemble
731 systems. Further, only a minor fraction of ensemble members reach the observed
732 precipitation intensities at noon. By investigating the structures of the precipitation
733 forecasts, further insight into the behavior of the ensemble systems is provided. The
734 number and volume of precipitation objects describe how models perform in a spatial
735 context. In this respect, AROME-EPS clearly shows more ability to replicate the real

736 spatial structure of precipitation. Although the number of objects in the region *Austria*
737 is too low during the first forecast hours, the further development as observed by the
738 INCA analysis in Figure 12b is described well. In the ALADIN-LAEF forecast the
739 number of precipitation objects is very low, mostly a product of the lower resolution.
740 The volumes of the precipitation events are in direct connection with their number
741 (not shown). ALADIN-LAEF overestimates the volumes to the same degree as it
742 underestimates their numbers. However, it shows a clear diurnal variation of the
743 volumes with a maximum around noon, which is not indicated by AROME.

744 The fact that ALADIN-LAEF tends to produce fewer but larger precipitation objects
745 does not lead to worse verification statistics for ALADIN-LAEF. On the contrary, in
746 most regions the hit rate is higher for ALADIN-LAEF than for AROME-EPS and the
747 number of missed events is lower. AROME-EPS, on the other hand outperforms
748 ALADIN-LAEF in terms of correct negatives and false alarms (not shown).

749 These results are also reflected in the temporal evolution of SAL-scores in Figure
750 12c. As expected, the structure score *S* is too high for ALADIN-LAEF, due to the
751 overestimation of the volumes of precipitation objects. At the same time, however,
752 AROME-EPS produces a low *S* score which means that it still produces too small
753 and peaked precipitation objects compared to INCA.

754 Interestingly, there is a late peak in the *S* score between 26-28 hours lead time in
755 both models, which follows a short minimum at 25 hours lead time. This is also
756 slightly reflected in the *A* score. The sequence of minimum and peak is related to a
757 nightly shower, which was also simulated by the ensembles, but with a delay of
758 approximately 2 hours. The location or *L*-score is rather constant in time for both

759 ensemble models. This means that they were able to reproduce the changing spatial
760 focus and distribution of precipitation during the day.

761 **5. Summary and conclusions**

762 In this paper we investigate the forecast performance of the 2.5 km convection-
763 permitting ensemble AROME-EPS by comparison with the regional 11 km ensemble
764 ALADIN-LAEF to reveal the benefit provided by a CP EPS. The regional EPS,
765 ALADIN-LAEF, involves several sources of forecast perturbations, such as initial
766 condition perturbations by blending ECMWF-EPS with ALADIN-LAEF breeding
767 vectors and assimilation of perturbed surface observations, and a multi-physics
768 scheme. The high-resolution, convection-permitting AROME-EPS solely performs
769 downscaling of the ALADIN-LAEF forecasts. The performance of the ensembles is
770 evaluated for a 3-month period during the convective season of 2011 and for a
771 typical convective day in April 2014 with a special focus on precipitation events in
772 mountainous terrain and lowland regions. The aim is to show whether the
773 convection-permitting ensemble provides benefits to the regional ensemble with deep
774 convection parameterization. The evaluation is conducted using a combination of
775 standard deterministic and probabilistic verification scores and selected spatial
776 verification measures. The former are applied on several main forecast parameters
777 for surface and upper levels, the latter – according to their definition – only for
778 precipitation.

779 The forecast quality for the main meteorological parameters (except precipitation) for
780 the surface and selected upper levels is strongly dependent on the model bias and is
781 rather balanced, except for diurnal variations near the surface. However,

782 characteristic differences are revealed by the investigation of the precipitation
783 forecasts. A known drawback of models using deep convection schemes proves true,
784 which is the premature onset of precipitation in the daily cycle by ALADIN-LAEF (see
785 e.g. Wittmann et al., 2010; Weusthoff et al., 2010). On the other hand, an
786 overestimation of precipitation intensities at the peak of convection activities by
787 AROME-EPS is also confirmed, which has been assumed in previous validations.
788 Both of these properties are found to be more pronounced in mountainous than in flat
789 regions.

790 ALADIN-LAEF shows skill in the prediction of probabilities for low precipitation
791 thresholds, i.e. to distinguish between *rain* and *no rain*. This is also true for small
792 scales, but it is again dependent on the time of day, as the early onset of precipitation
793 has a negative influence on the verification scores. AROME-EPS, on the other hand,
794 has a better ability to capture the diurnal cycle of convective precipitation, especially
795 over mountainous terrain. At small spatial scales, it further demonstrates better
796 performance for higher precipitation thresholds. The results of the evaluations in this
797 study lead to the conclusion, that the convection permitting ensemble is more skillful
798 on the precipitation forecast than its mesoscale counterpart, the regional ensemble.
799 The positive impact is larger for the mountainous areas than for the lowlands.
800 Nevertheless, the knowledge of which precipitation situations can be better modeled
801 by the convection-permitting ensemble is important to have. For many applications,
802 e.g. for large-scale extreme events, such as the Central Europe flooding event of
803 2013, the best solution will be a combination of both systems: the coarser ensembles
804 with longer forecast range for (pre)-warnings, and the convection-permitting

805 ensemble for the detailed specification of the expected event. Regarding different
806 time and length-scales in that way could lead to the generation of *seamless* forecast
807 products (e.g. Drobinski et al. 2014, Vitart et al. 2008).

808 This study is considered as initial point for further investigations and improvement of
809 the convection-permitting ensemble AROME-EPS. The low spread of the prevailing
810 AROME-EPS version is a clear drawback compared to ALADIN-LAEF. Therefore,
811 future enhancements of AROME-EPS will involve components, which will
812 presumably increase ensemble spread. Among those upgrades will be ensemble
813 data assimilation and physics perturbations (multi-model and stochastic). The
814 expectation with these components is that forecast errors will be reduced, and that a
815 more realistic simulation of forecast uncertainties will be achieved.

816 **6. Code and/or data availability**

817 The ALADIN-LAEF and AROME codes including all related intellectual property
818 rights, are owned by the members of the LACE consortium and ALADIN consortium.
819 Access to the ALADIN-LAEF and AROME systems, or elements thereof, can be
820 granted upon request and for research purposes only. INCA and INCA data are only
821 available subject to a licence agreement with ZAMG.

822

823 Acknowledgments

824 We gratefully acknowledge all the LACE/ALADIN/HIRLAM colleagues who have
825 contributed to the development of AROME. ECMWF has provided the computer

826 facilities and technical help implementing ALADIN-LAEF and AROME-EPS on the
827 ECMWF HPCF.

828 REFERENCES

829 Ahijevych D., E. Gilleland, B. Brown, and E. Ebert, 2009: Application of spatial
830 forecast verification methods to gridded precipitation forecasts. *Wea. Forecasting*,
831 **24**, 1485–1497.

832 Aligo A. E., W. A. Gallus Jr., and M. Segal, 2009: On the Impact of WRF Model
833 Vertical Grid Resolution on Midwest Summer Rainfall Forecasts. *Wea. Forecasting*,
834 **24**, 575-594.

835 Barthlott C., R. Burton, D. Kirshbaum, K. Hanley, R. Richard, J. P. Chaboreau, J.
836 Trentmann, B. Kern, H.-S. Bauer, T. Schwitalla, C. Keil, Y. Seity, A. Gadian, A. M.
837 Blyth, S. Mobbs, C. Flamant, and J. Handwerker, 2011: Initiation of deep convection
838 at marginal instability in an ensemble of mesoscale models: A case-study from
839 COPS. *Quart. J. Roy. Meteor. Soc.*, **137**, 118–136.

840 Bauer H.S., T. Weusthoff, M. Dorninger, V. Wulfmeyer, T. Schwitalla, T. Gorgas, M.
841 Arpagaus, and K. Warrach-Sagi, 2011: Predictive skill of a subset of models
842 participating in D-PHASE in the COPS region. *Q. J. R. Meteorol. Soc.* **137**, 287-305.

843 Bechtold, P., N. Semane, P. Lopez, and J.-P. Chaboureaud, A. Beljaars, N. Bormann,
844 2013: Breakthrough in forecasting equilibrium and non-equilibrium convection.
845 *ECMWF Newsletter*, **136**, 15-22.

846 Bowler, N. E., A. Arribas, K. R. Mylne, K. B. Robertson, and S. E. Beare, 2008: The

- 847 MOGREPS short-range ensemble prediction system. *Quart. J. Roy. Meteor. Soc.*,
848 **134**, 703–722.
- 849 Ben Bouallégue, Z., S. E. Theis, and C. Gebhardt, 2013: Enhancing COSMO-DE
850 ensemble forecasts by inexpensive techniques. *Meteor. Z.*, **22**, 49–59.
- 851 Bougeault, P., 1985: A simple parameterization of the large-scale effects of cumulus
852 convection. *Mon. Wea. Rev.*, **113**, 2108–2121.
- 853 Bouttier, F., B. Vié, O. Nuissier, and L. Raynaud, 2012: Impact of Stochastic Physics
854 in a Convection-Permitting Ensemble. *Mon. Wea. Rev.*, **140**, 3706–3721.
- 855 Brier, G. W., 1950: Verification of forecasts expressed in terms of probability. *Mon.*
856 *Wea. Rev.*, **78**, 1–3.
- 857 Bryan, G. H., J. C. Wyngaard, and J. M. Fritsch, 2003: Resolution requirements for
858 the simulation of deep moist convection. *Mon. Wea. Rev.*, **131**, 2394–2416.
- 859 Bukovsky, M. S., J. S. Kain and M. E. Baldwin, 2006: Bowing convective systems in
860 a popular operational model: Are they for real? *Wea. Forecasting*, **21**, 307–324.
- 861 Caron, J., 2013: Mismatching perturbations at the lateral boundaries in limited-
862 areaensemble forecasting: A case study. *Mon. Wea. Rev.*, **141**, 356–374. Casati B. L,
863 L. J. Wilson, D. B. Stephenson, P. Nurmi, A. Ghelli, M. Pocerich, U. Damrath, E. E.
864 Ebert, B. G. Brown, and S. Mason, 2008: Review forecast verification: current status
865 and future directions. *Meteor. Appl.*, **15**, 3–18.

- 866 Clark, A. J., W. A. Gallus Jr., and T.-C. Chen, 2007: Comparison of the Diurnal
867 Precipitation Cycle in Convection-Resolving and Non-Convection-Resolving
868 Mesoscale Models. *Mon. Wea. Rev.*, **135**, 3456-3473.
- 869 Clark, A. J., W. A. Gallus Jr., M. Xue, and F. Kong, 2009: A Comparison of
870 Precipitation Forecast Skill between Small Convection-Allowing and Large
871 Convection-Parameterizing Ensembles. *Wea. Forecasting*, **24**, 1121-1140.
- 872 Clark, A. J., J. S. Kain, D. J. Stensrud, M. Xue, F. Kong, M. C. Coniglio, K. W.
873 Thomas, Y. Wang, K. Brewster, J. Gao, X. Wang, S. J. Weiss and J. Du, 2011:
874 Probabilistic Precipitation Forecast Skill as a Function of Ensemble Size and Spatial
875 Scale in a Convection-Allowing Ensemble. *Mon. Wea. Rev.*, **139**: 1410-1418.
- 876 Davis, C. A., K. W. Manning, R. E. Carbone, S. B. Trier, and J. D. Tuttle, 2003:
877 Coherence of warm season continental rainfall in numerical weather prediction
878 models. *Mon. Wea. Rev.*, **131**, 2667–2679.
- 879 Davison, A.C. and D.V. Hinkley, 1997: Bootstrap Methods and their applications –
880 Cambridge University Press, Cambridge, UK, 193 f.
- 881 Done, J. M., G. C. Craig, S. L. Gray, P. A. Clark, and M. E. B. Gray, 2006:
882 Mesoscale simulations of organized convection: Importance of convective
883 equilibrium. *Quart. J. Roy. Meteor. Soc.*, **132**, 737–756.
- 884 Drobinski, P., and Coauthors, 2014: HyMeX: A 10-Year Multidisciplinary Program on
885 the Mediterranean Water Cycle. *Bull. Amer. Meteor. Soc.*, **95**, 1063-1082.

- 886 Ferro, C.A.T., 2007: A probability model for verifying deterministic forecasts of
887 extreme events. *Wea. Forecasting*, **22**, 1089–1100.
- 888 Gebhardt, C., S. E. Theis, M. Paulat and Z. Ben Bouallègue, 2011: Uncertainties in
889 COSMO-DE precipitation forecasts introduced by model perturbations and variation
890 of lateral boundaries. *Atmos. Res.*, **100**, 168-177
- 891 Geleyn, J.-F., B. Catry, Y. Bouteloup, and R. Brožková, 2008: A statistical approach
892 for sedimentation inside a microphysical precipitation scheme. *Tellus*, **60A**, 649–662,
893 doi:10.1111/j.1600-0870.2008.00323.x.
- 894 Gerard, L., J.-M. Piriou, R. Brožkova, J.-F. Geleyn, and D. Banciu, 2009: Cloud and
895 precipitation parameterization in a meso-gamma scale operational weather prediction
896 model. *Mon. Wea. Rev.*, **137**, 3960–3977.
- 897 Gilleland, E., D. A. Ahijevych, B. G. Brown, and E. E. Ebert, 2010: Verifying forecasts
898 spatially. *Bull. Amer. Meteor. Soc.*, **47**, 1365–1373.
- 899 Gneiting, T., and A. E. Raftery, 2007: Strictly Proper Scoring Rules, Prediction and
900 Estimation. *Journal of the American Statistical Association*, **102**, 359-378.
- 901 Haiden, T., and G. Pistotnik, 2009: Intensity-dependent parameterization of elevation
902 effects in precipitation analysis. *Adv. Geosci.*, **20**, 33-38.
- 903 Haiden, T., A. Kann, C. Wittmann, G. Pistotnik, B. Bica, and C. Gruber, 2011: The
904 Integrated Nowcasting through Comprehensive Analysis (INCA) System and Its
905 Validation over the Eastern Alpine Region. *Wea. Forecasting*, **26**, 166-183.

- 906 Haiden, T., L. Magnusson, I. Tsonevsky, F. Wetterhall, L. Alfieri, F. Pappenberger, P.
907 de Rosnay, J. Muñoz-Sabater, G. Balsamo, C. Albergel, R. Forbes, T. Hewson, S.
908 Malardel, and D. Richardson, 2014: ECMWF forecast performance during the June
909 2013 flood in Central Europe. *ECMWF – Technical Memorandum*, **723**,
910 <http://old.ecmwf.int/publications/library/ecpublications/pdf/tm/701-800/tm723.pdf> (Sep
911 2, 2014).
- 912 Hanley, K. E., D. J. Kirshbaum, N. M. Roberts and G. Leoncini, 2013: Sensitivities of
913 a Squall Line over Central Europe in a Convective-Scale Ensemble. *Mon. Wea. Rev.*,
914 **141**, 112-133.
- 915 Hersbach, H., 2000: Decomposition of the Continuous Ranked Probability Score for
916 Ensemble Prediction Systems. *Wea. Forecasting*, **15**, 559-570.
- 917 Jolliffe, I., 2007: Uncertainty and inference for verification measures. *Wea.*
918 *Forecasting*, **22**, 637–650.
- 919 Kühnlein, C., C. Keil, G. C. Craig, and C. Gebhardt, 2014: The impact of downscaled
920 initial condition perturbations on convective-scale ensemble forecasts of precipitation.
921 *Quart. J. Roy. Meteor. Soc.*, **140**, 1552–1562.
- 922 Liu, C., M. W. Moncrieff, J. D. Tuttle, and R. E. Carbone, 2006 : Explicit an
923 Parameterized Episodes of Warm-Season Precipitation over the Continental United
924 States. *Adv. Atmos. Sci.*, **23**, 91-105.
- 925 Masson, V., 2000: A physically-based scheme for the urban energy budget in
926 atmospheric models. *Bound.-Layer Meteor.*, **94**, 357–397.

- 927 Mlawer, E. J., S. J. Taubman, P. D. Brown, M. J. Iacono, and S. A. Clough, 1997 :
928 Radiative transfer for inhomogeneous atmospheres: RRTM, a validated correlated-k
929 model for the longwave. *J. Geophys. Res.*, **102D**, 16663–16682.
- 930 Morcrette, J.-J., 1991 : Radiation and cloud radiative properties in the ECMWF
931 operational weather forecast model. *J. Geophys. Res.*, **96D**, 9121–9132.
- 932 Murphy, A. H., 1973: A new vector partition of the probability score. *J. Appl. Meteor.*,
933 **12**, 595–600.
- 934 Nurmi, P., 2003: Recommendations on the verification of local weather forecasts.
935 *ECMWF Technical Memoranda*, **430**, 19 pp. [available online at
936 <http://old.ecmwf.int/publications/library/do/references/show?id=86094>] (Oct 20,
937 2014).
- 938 Peralta, C., Z. Ben Bouallègue, S. E. Theis, C. Gebhardt, and M. Buchhold, 2012:
939 Accounting for initial condition uncertainties in COSMO-DE-EPS. *J. Geophys. Res.*,
940 **117**, 1–13, doi: 10.1029/2011JD016581.
- 941 Pergaud, J., V. Masson, V., and S. Malardel, 2009: A parameterization of dry
942 thermals and shallow cumuli for mesoscale numerical weather prediction, *Bound.-*
943 *Layer Meteor.*, **132**, 83–106.
- 944 Pinty, J. P., and Jabouille, P., 1998: A mixed phase cloud parameterization for use in
945 a mesoscale nonhydrostatic model: Simulations of a squall line and of orographic
946 precipitation. *Preprints, Conf. on Cloud Physics*, Everett, WA, Amer. Meteor. Soc.,
947 217–220.

- 948 Richard E., Buzzi A., and Zängl G., 2007: Quantitative precipitation forecasting in the
949 Alps: The advances achieved by the Mesoscale Alpine Programme. *Q. J. R.*
950 *Meteorol. Soc.* **133**: 831–846.
- 951 Ritter, B., and J.-F. Geleyn, 1992: A comprehensive radiation scheme for numerical
952 weather prediction models with potential applications in climate simulations. *Mon.*
953 *Wea. Rev.*, **120**, 303–325.
- 954 Roberts, N. M., and H. W. Lean, 2008: Scale-selective verification of rainfall
955 accumulations from high-resolution forecasts of convective events. *Mon. Wea. Rev.*,
956 **136**, 78–97.
- 957 Romine, G. S., C. S. Schwartz, J. Berner, K. R. Fossell, C. Snyder, J. L. Anderson,
958 M. L. Weisman, 2014: Representing Forecast Error in a Convection-Permitting
959 Ensemble System. *Mon. Wea. Rev.*, **142**, 4519-4541.
- 960 Rotach, M. W., and Coauthors including and T. Gorgas and Y. Wang, 2009: MAP D-
961 PHASE real time demonstration of weather forecast quality in the Alpine region. *Bull.*
962 *Amer. Meteor. Soc.*, **90**: 1321-1336.
- 963 Schumacher, R. S., A. J. Clark, M. Xue, and F. Kong, 2013: Factors Influencing the
964 Development and Maintenance of Nocturnal Heavy-Rain-Producing Convective
965 Systems in a Storm-Scale Ensemble. *Mon. Wea. Rev.*, **141**: 2778-2801.
- 966 Schumacher, R. S., and A. J. Clark, 2014: Evaluation of ensemble configurations for
967 the analysis and prediction of heavy-rain-producing mesoscale convective systems.
968 *Mon. Wea. Rev.*, **e-View**, doi: <http://dx.doi.org/10.1175/MWR-D-13-00357.1>.

969 Schwartz C. S., J. S. Kain, S. J. Weiss, M. Xue, D. R. Bright, F. Kong, K. W. Thomas,
970 J. J. Levit, M. C. Coniglio, M. S. Wandishin, 2010: Toward Improved Convection-
971 Allowing Ensembles: Model Physics Sensitivities and Optimizing Probabilistic
972 Guidance with Small Ensemble Membership. *Wea. Forecasting*, **25**, 263–280.
973 DOI:10.1175/2009WAF2222267.1.

974 Schwartz, C. S., G. S. Romine, K. R. Smith, and M. L. Weisman, 2014:
975 Characterizing and optimizing precipitation forecasts from a convection-permitting
976 ensemble initialized by a mesoscale ensemble kalman filter. *Wea. Forecasting*, **29**,
977 1295–1318.

978 Seity, Y., P. Brousseau, S. Malardel, G. Hello, P. Bénard, F. Bouttier, C. Lac, and V.
979 Masson, 2011: The AROME-France Convective-Scale Operational Model. *Mon.*
980 *Wea. Rev.* **139**: 976–991.

981 Tailleurfer, F., 2002: CANARI – Technical Documentation - Based on ARPEGE cycle
982 CY25T1 (AL25T1 for ALADIN), [available online at:
983 http://www.cnrm.meteo.fr/gmapdoc/IMG/ps/canari_doc_cy25t1.ps (cited Dec 14,
984 2015)]

985 Taraphdar, S., P. Mukhopadhyay, L. R. Leung, F. Zhang, S. Abhilash, and B. N.
986 Goswami, 2014: The role of moist processes in the intrinsic predictability of Indian
987 Ocean cyclones, *J. Geophys. Res. Atmos.*, **119**, 8032-8048,
988 doi:10.1002/2013JD021265

989 Tennant, W., 2015: Improving initial condition perturbations for MOGREPS-UK.
990 *Quart. J. Roy. Meteor. Soc.*, DOI: 10.1002/qj.2524. Online publication date: 1-Feb-2015.

- 991 Theis, S. E., A. Hense, U. Damrath, 2005: Probabilistic precipitation forecasts from a
992 deterministic model: a pragmatic approach. *Meteor. Appl.* **12**, 257–268.
993 DOI:10.1017/S1350482705001763.
- 994 Toth, Z., and E. Kalnay, 1993: Ensemble forecasting at NMC: the generation of
995 perturbation. *Bull. Amer. Meteor. Soc.*, **74**, 2317-2330.
- 996 UK Met Office, July 2014 (cited Oct 21, 2014): Benefits of high resolution ensemble
997 forecasts. [available online at [http://www.metoffice.gov.uk/research/news/2014/high-](http://www.metoffice.gov.uk/research/news/2014/high-resolution-ensembles)
998 [resolution-ensembles](http://www.metoffice.gov.uk/research/news/2014/high-resolution-ensembles)]
- 999 Vana F., P. Benard, J.-F. Geleyn, A. Simon, and Y. Seity, 2008: Semi-Lagrangian
1000 advection scheme with controlled damping: an alternative to nonlinear horizontal
1001 diffusion in a numerical weather prediction model. *Quart. J. Roy. Meteor. Soc.*, **134**,
1002 523–537.
- 1003 Vié, B., G. Molinié, O. Nussier, B. Vincendon, V. Ducrocq, F. Bouttier, and E.
1004 Richard, 2012: Hydro-meteorological evaluation of a convection-permitting ensemble
1005 prediction system for Mediterranean heavy precipitating events. *Nat. Hazards Earth*
1006 *Syst. Sci.*, **12**: 2631–2645.
- 1007
- 1008 Vitart F., R. Buizza, M. A. Balmaseda, G. Balsamo, J.-R. Bidlot, A. Bonet, M.
1009 Fuentes, A. Hofstadler, F. Molteni, and T. N. Palmer, 2008: The new VarEPS–
1010 monthly forecasting system: A first step towards seamless prediction. *Quart. J. Roy.*
1011 *Meteor. Soc.*, **134**, 1789–1799.

- 1012 Wang, Y., A. Kann, M. Bellus, J. Pailleux, and C. Wittmann, 2010: A strategy for
1013 perturbing surface initial conditions in LAMEPS. *Atmos. Sci. Let.*, **11**, 108-113.
- 1014 Wang, Y., M. Bellus, C. Wittmann, M. Steinheimer, F. Weidle, A. Kann, S. Ivatek-
1015 Šahdan, W. Tian, X. Ma, S. Tascu, and E. Bazile, 2011: The Central European
1016 limited-area ensemble forecasting system: ALADIN-LAEF. *Quart. J. Roy. Meteor.
1017 Soc.*, **137**, 483–502.
- 1018 Wang, Y., S. Tascu, F. Weidle, and K. Schmeisser, 2012: Evaluation of the Added
1019 Value of Regional Ensemble Forecasts on Global Ensemble Forecasts. *Wea.
1020 Forecasting*, **27**, 972-987.
- 1021 Wang Y., M. Bellus, J.-F. Geleyn, X. Ma, W. Tian, and F. Weidle, 2014: A New
1022 Method for Generating Initial Condition Perturbations in a Regional Ensemble
1023 Prediction System: Blending. *Mon. Wea. Rev.*, **142**, 2043-2059.
- 1024 Weckwerth, T., L. Bennett, L. Miller, J. Van Baelen, P. Di Girolamo, A. Blyth, and T.
1025 Hertneky, 2014: An Observational and Modeling Study of the Processes Leading to
1026 Deep, Moist Convection in Complex Terrain. *Mon. Wea. Rev.*, **142**, 2687-2708.
- 1027 Weidle, F., Y. Wang, W. Tian and T. Wang, 2013: Validation of Strategies using
1028 Clustering Analysis of ECMWF EPS for Initial Perturbations in a Limited Area Model
1029 Ensemble Prediction System. *Atmosphere-Ocean*, **51**, 284-295.
- 1030 Weisman, M. L., W. C. Skamarock, and J. B. Klemp, 1997: The resolution
1031 dependence of explicitly modeled convective systems. *Mon. Wea. Rev.*, **125**, 527–
1032 548.

- 1033 Wernli, H., M. Paulat, M. Hagen, and C. Frei, 2008: SAL - A Novel Quality Measure
1034 for the Verification of Quantitative Precipitation Forecasts. *Mon. Wea. Rev.*, **136**,
1035 4470–4487.
- 1036 Weusthoff, T., F. Ament, M. Arpagaus, and M. W. Rotach, 2010: Assessing the
1037 Benefits of Convection-Permitting Models by Neighborhood Verification: Examples
1038 from MAP D-PHASE. *Mon. Wea. Rev.*, **138**, 3418–3433.
- 1039 Wilks, D. S., 1997: Resampling hypothesis testing for autocorrelated fields.
1040 *J.Climate*, 10, 65-82.
- 1041 Wilks, D. S., 2006: *Statistical Methods in the Atmospheric Sciences*, 2nd Ed.,
1042 London, Academic Press, 627 pp.
- 1043 Wittmann, C., T. Haiden, and A. Kann, 2010: Evaluating multi-scale precipitation
1044 forecasts using high resolution analysis. *Adv. Sci. Res.*, **4**, 89-98, DOI:10.5194/asr-4-
1045 89-2010.
- 1046 Wulfmeyer V., and Coauthors, 2008: The Convective and Orographically induced
1047 Precipitation Study: A research and development project of the World Weather
1048 Research Program for improving quantitative precipitation forecasting in low-
1049 mountain regions. *Bull. Am. Meteorol. Soc.* **89**: 1477–1486,
1050 DOI:10.1175/2008BAMS2367.1.
- 1051 Wulfmeyer, V., and Coauthors including T. Gorgas and Y. Wang, 2011: The
1052 Convective and Orographically-induced Precipitation Study (COPS): the scientific

1053 strategy, the field phase, and research highlights. *Quart. J. Roy. Meteor. Soc.* **137**:
1054 3–30.

1055 Xue, M., and Coauthors, 2007: CAPS realtime storm-scale ensemble and high-
1056 resolution forecasts as part of the NOAA Hazardous Weather Testbed 2007 spring
1057 experiment. *Extended Abstracts, 22nd Conference on Weather Analysis and*
1058 *Forecasting/18th Conference on Numerical Weather Prediction*, Park City, UT. Amer.
1059 Meteor. Soc., [Available online at <http://ams.confex.com/ams/pdfpapers/124587.pdf>].

1060 Xue, M., and Coauthors, 2009: CAPS realtime multi-model convection-allowing
1061 ensemble and 1-km convection-resolving forecasts for the NOAA Hazardous
1062 Weather Testbed 2009 spring experiment. Preprints, *23rd Conf. on Weather Analysis*
1063 *and Forecasting/19th Conf. on Numerical Weather Prediction*, Omaha, NE, Amer.
1064 Meteor. Soc., 16A.2. [Available online at [http://ams.confex.com/ams/23WAF19NWP/](http://ams.confex.com/ams/23WAF19NWP/techprogram/paper_154323.htm)
1065 [techprogram/paper_154323.htm](http://ams.confex.com/ams/23WAF19NWP/techprogram/paper_154323.htm).]

1066 Zhu, Y., Z. Toth, R. Wobus, D. Richardson, and K. Mylne, 2002: The Economic Value
1067 Of Ensemble-Based Weather Forecasts. *Bull. Amer. Meteor. Soc.* **83**, 73-83.

1068

1069

1070

	ALADIN-LAEF	AROME-EPS
Ensemble size	16+1 members	16 members
Horizontal resolution	11 km	2.5 km
Vertical resolution	45 layers	60 layers
Model time step	450 s	60 s
Coupling-Model	ECMWF-EPS	ALADIN-LAEF
Coupling-Update	6 h	3 h
No. of grid points	206 x 164	432 x 320
Forecast range	72 h	30 h
Runs/Day	2 (0000, 1200 UTC)	1 (0000 UTC)

1071

1072 **Table 1:** Main characteristics of the ALADIN-LAEF and AROME-EPS.

1073

1074

1075

1076

1077

1078

← **Formatiert:** Links, Abstand Nach: 0 Pt., Tabstops: Nicht an 14,92 cm + 16 cm

1079 | Figure 1: Geographic domains and topographies of a) ALADIN-LAEF, where the red
1080 | frame is the output domain used for the present study, and b) AROME-EPS, which is
1081 | shown by the blue frame in (a).

1082

1083 | Figure 2: Locations of meteorological surface observation stations within the
1084 | evaluation domain.

1085

1086 | Figure 3: INCA domain and topography with the sub-domains, which are used for the
1087 | evaluation.

1088

1089 | Figure 4: Bias (left panel) and CRPS (right panel) for 2m relative humidity (top), 2m
1090 | temperature (middle) and 10m wind speed (bottom) for the period of May 15 –
1091 | August 15, 2011 of AROME-EPS (dotted line) and ALADIN-LAEF (solid line), both
1092 | verified over the AROME-domain. Lead times, which are marked with asterisks (*)
1093 | indicate results with significant differences between the ensembles.

1094 | ~~Figure 4: Bias (left panel) and CRPS (right panel) for 2m relative humidity (top), 2m~~
1095 | ~~temperature (middle) and 10m wind speed (bottom) for the period of May 15 –~~
1096 | ~~August 15, 2011 in the AROME-domain of AROME-EPS (dotted line) and ALADIN-~~
1097 | ~~LAEF (solid line). Lead times, which are marked with asterisks (*) indicate results~~
1098 | ~~with significant differences between the ensembles.~~

1099

1100 Figure 5: Time evolution of 3-hourly accumulated precipitation forecast for INCA
1101 (solid line), ALADIN-LAEF ensemble mean (dashed line) and AROME-EPS
1102 ensemble mean (dotted line) for regions *Austria* (top), *West* (middle) and *Northeast*
1103 (bottom). Left panels show results for the days with strong synoptic forcing, right
1104 panels for weak synoptic forcing. The shaded areas denote the range of individual
1105 ensemble member forecasts for ALADIN-LAEF (dark grey) and AROME-EPS (light
1106 grey) respectively.

1107
1108 Figure 6: Time evolution of the Brier Score with confidence intervals (shades) for
1109 region *Austria*, AROME-EPS (dotted line) and ALADIN-LAEF (dashed line). a) strong
1110 synoptic forcing and precipitation threshold 0.1 mm / 3 h, b) weak synoptic forcing
1111 and 0.1 mm / 3 h, c) strong synoptic forcing and 2 mm / 3 h, and d) weak synoptic
1112 forcing and 2 mm / 3 h.

1113
1114 Figure 7: Time evolution of SAL scores for AROME-EPS (left) and ALADIN-LAEF
1115 (right) for different forecast ranges in region *West*. Upper panels a) and b) show
1116 results for days with strong synoptic forcing; lower panels c) and d) for weak synoptic
1117 forcing. The boxes are created based on the scores of all individual ensemble
1118 members.

1119
1120 Figure 8: Same as in Figure 7, but for region *Northeast*.

1121

1122 Figure 9: Distances [km] between the centers of mass of the precipitation objects in
1123 the forecast and analysis fields for AROME-EPS (dotted) and ALADIN-LAEF
1124 (dashed) for thresholds of a) 0.1 mm / 3 h, and b) 2 mm / 3 h.

1125
1126 Figure 10: Fractional skill scores for a) strong synoptic forcing, and b) weak synoptic
1127 forcing of AROME-EPS (dashed) and ALADIN-LAEF (solid line) for the region
1128 *Austria*. Numbers denote the precipitation thresholds [mm]. The values represent
1129 averages for all hours of lead-time.

1130
1131 Figure 11: Observed (INCA, first column) and forecast (AROME-EPS and ALADIN-
1132 LAEF, second and third column, respectively) development of precipitation on 29
1133 April 2014 shown for selected times (rows). The panels show 1-hourly accumulated
1134 precipitation sums [mm].

1135
1136 Figure 12: Characteristics of the precipitation forecasts of ALADIN-LAEF and
1137 AROME-EPS on 29 April 2014. a) Temporal evolution of the mean areal precipitation
1138 compared with INCA, and b) temporal evolution of the number of precipitation
1139 objects. Dashed and dotted lines represent the ensemble mean and grey shades the
1140 ensemble spread. c) Temporal evolution of S (structure), A (amplitude) and L
1141 (location) scores of the ensemble means of ALADIN-LAEF (black) and AROME-EPS
1142 (grey).

1143

1144

1145

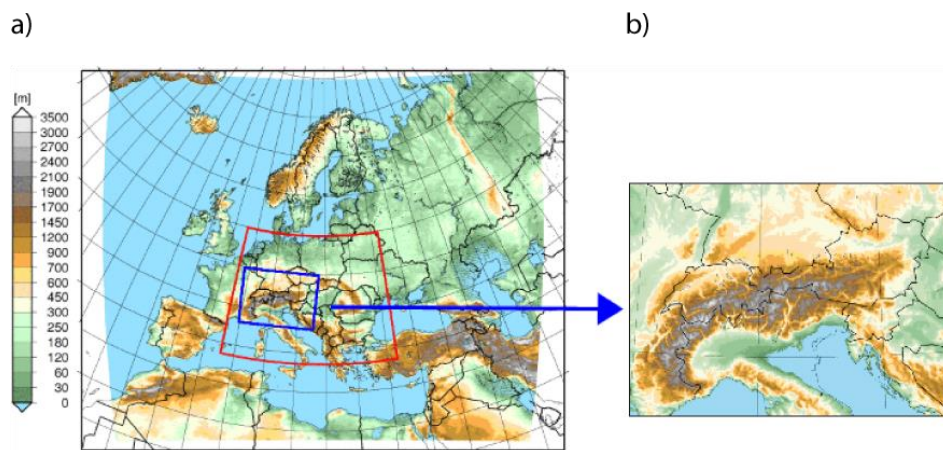
1146

1147

1148

1149

1150



1151

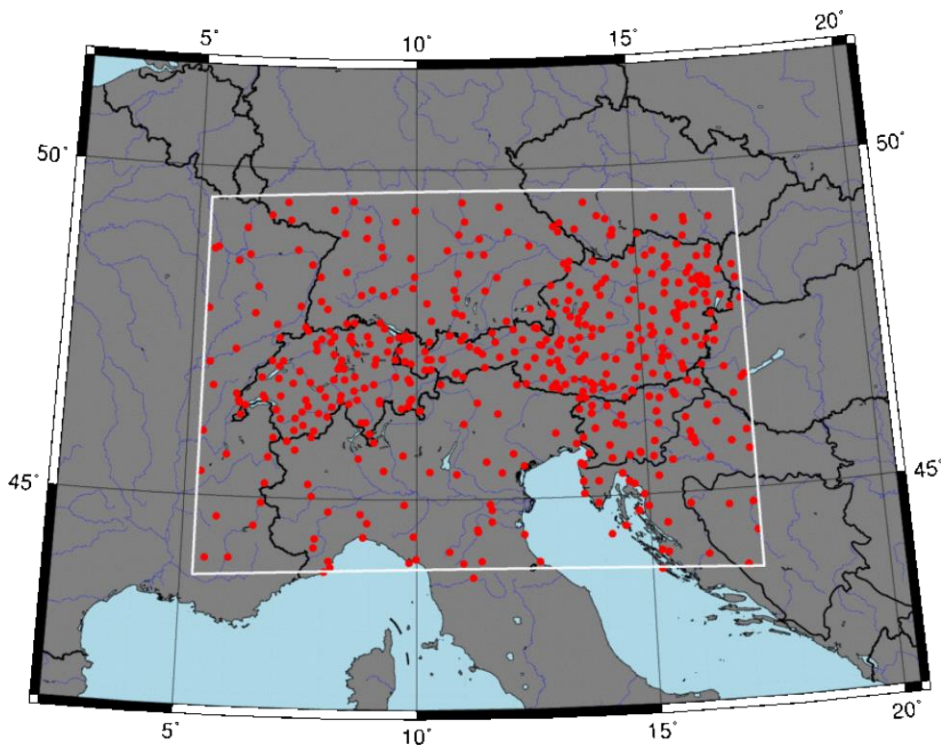
1152 Figure 1: Geographic domains and topographies of a) ALADIN-LAEF, where the red
1153 frame is the output domain used for the present study, and b) AROME-EPS, which is
1154 shown by the blue frame in (a).

1155

1156

1157

1158



1159

1160

1161 Figure 2: Locations of meteorological surface observation stations within the
1162 evaluation domain.

1163

1164

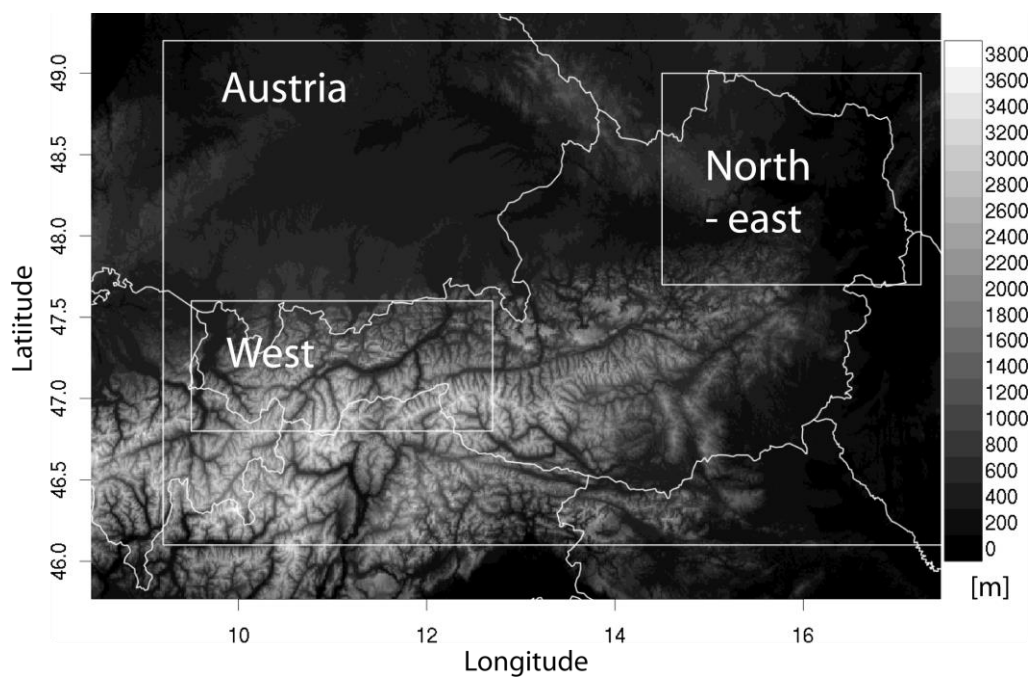
1165

1166

1167

1168

1169



1170

1171 Figure 3: INCA domain and topography with the sub-domains, which are used for the
1172 evaluation.

1173

1174

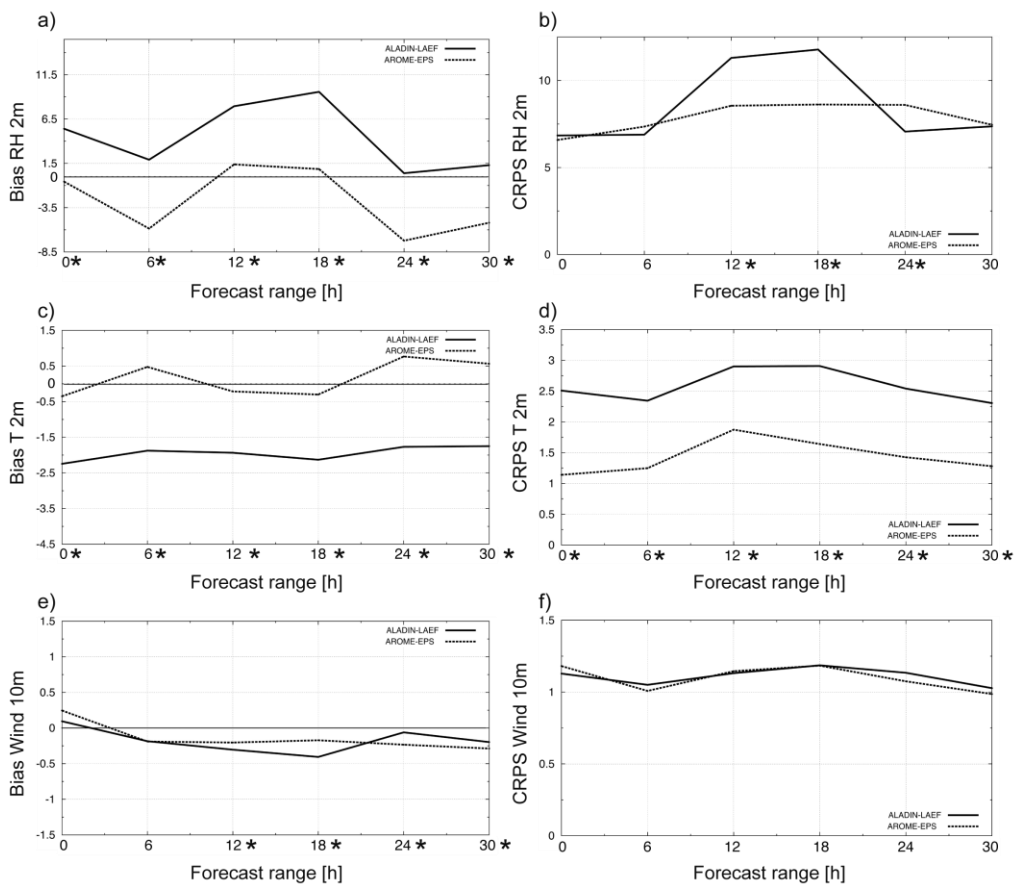
1175

1176

1177

1178

1179



1180

1181 Figure 4: Bias (left panel) and CRPS (right panel) for 2m relative humidity (top), 2m
 1182 temperature (middle) and 10m wind speed (bottom) for the period of May 15 –
 1183 August 15, 2011 in the AROME-domain of AROME-EPS (dotted line) and ALADIN-
 1184 LAEF (solid line), both verified over the AROME-domain. Lead times, which are
 1185 marked with asterisks (*) indicate results with significant differences between the
 1186 ensembles.

Formatiert: Schriftart: (Standard)
 Arial, 12 Pt., Nicht Fett, Schriftartfarbe:
 Automatisch

1187

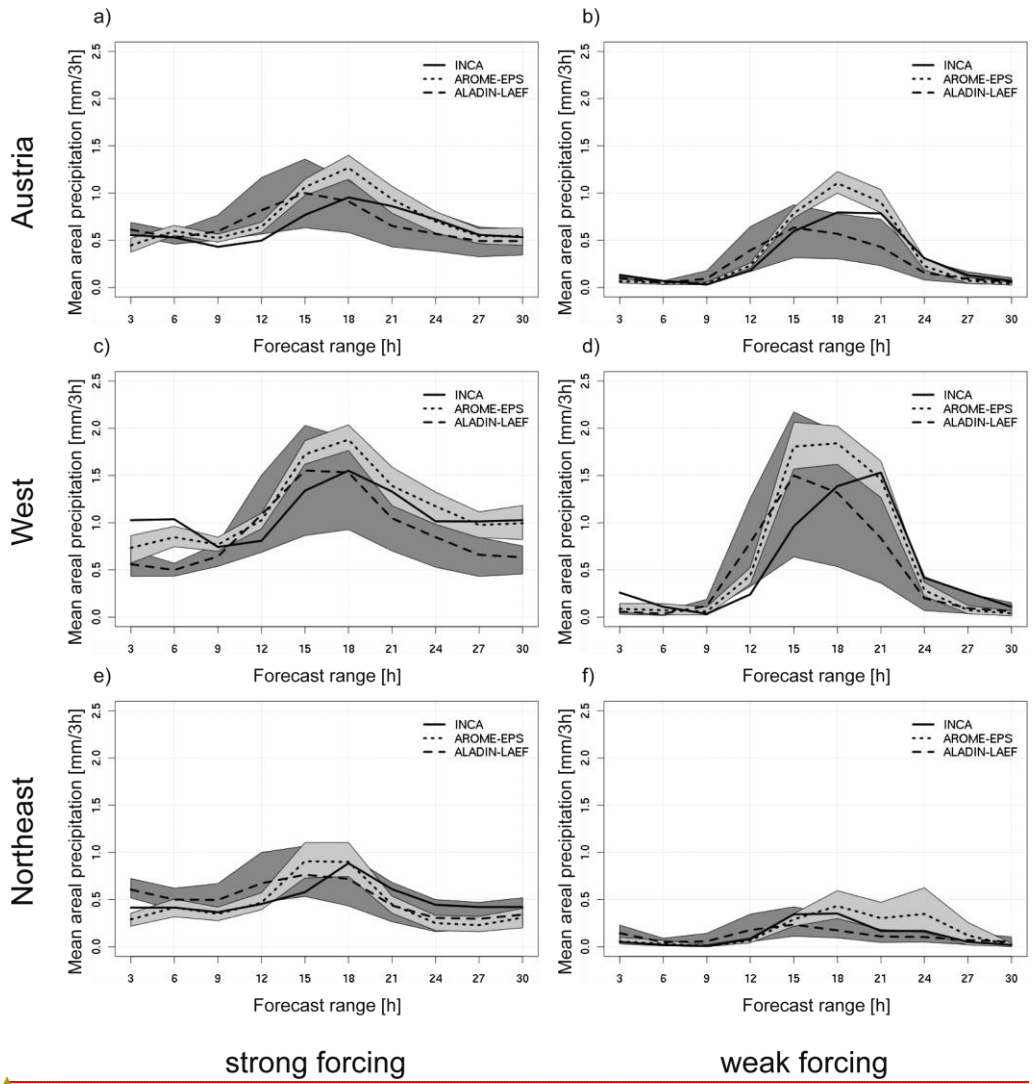
1188

1189

Formatiert: Schriftart: 11 Pt., Deutsch (Österreich)

Formatiert: Links, Zeilenabstand: Mehrere 1,15 ze

Formatiert: Schriftart: (Standard) Arial, 12 Pt., Nicht Fett, Schriftartfarbe: Automatisch



1190

strong forcing

weak forcing

1191 Figure 5: Time evolution of 3-hourly accumulated precipitation forecast for INCA

1192 (solid line), ALADIN-LAEF ensemble mean (dashed line) and AROME-EPS

1193 ensemble mean (dotted line) for regions *Austria* (top), *West* (middle) and *Northeast*
1194 (bottom). Left panels show results for the days with strong synoptic forcing, right
1195 panels for weak synoptic forcing. The shaded areas denote the range of individual
1196 ensemble member forecasts for ALADIN-LAEF (dark grey) and AROME-EPS (light
1197 grey) respectively.

1198

1199

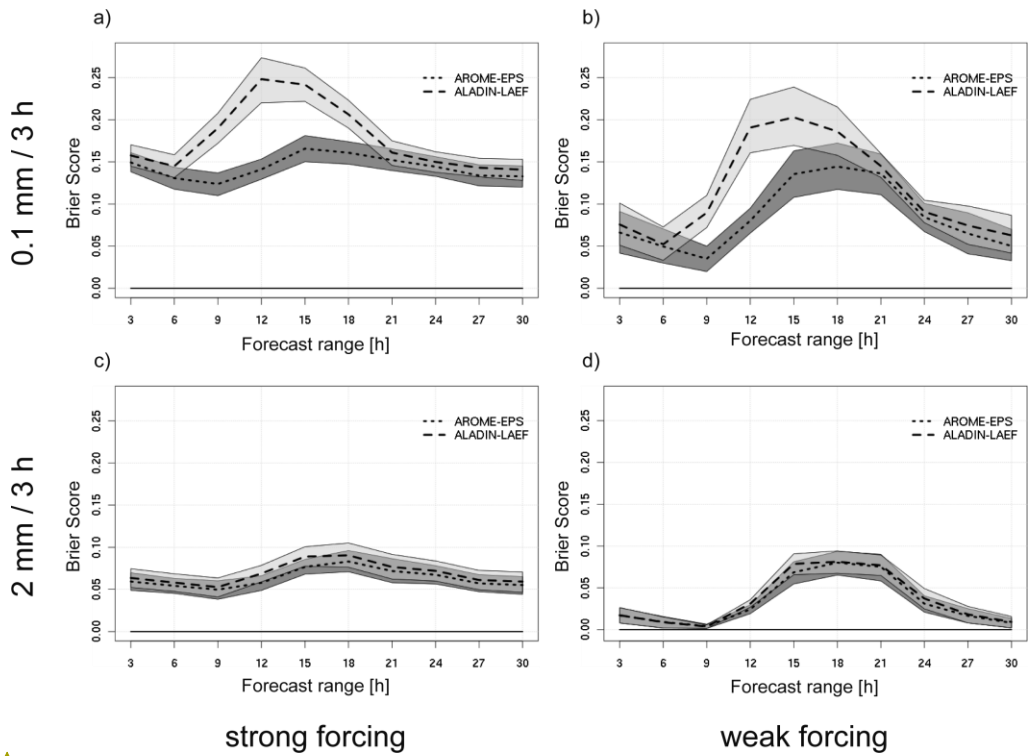
1200

1201

1202

1203

1204



Formatiert: Schriftart: (Standard)
Arial, 12 Pt., Nicht Fett, Schriftartfarbe:
Schwarz

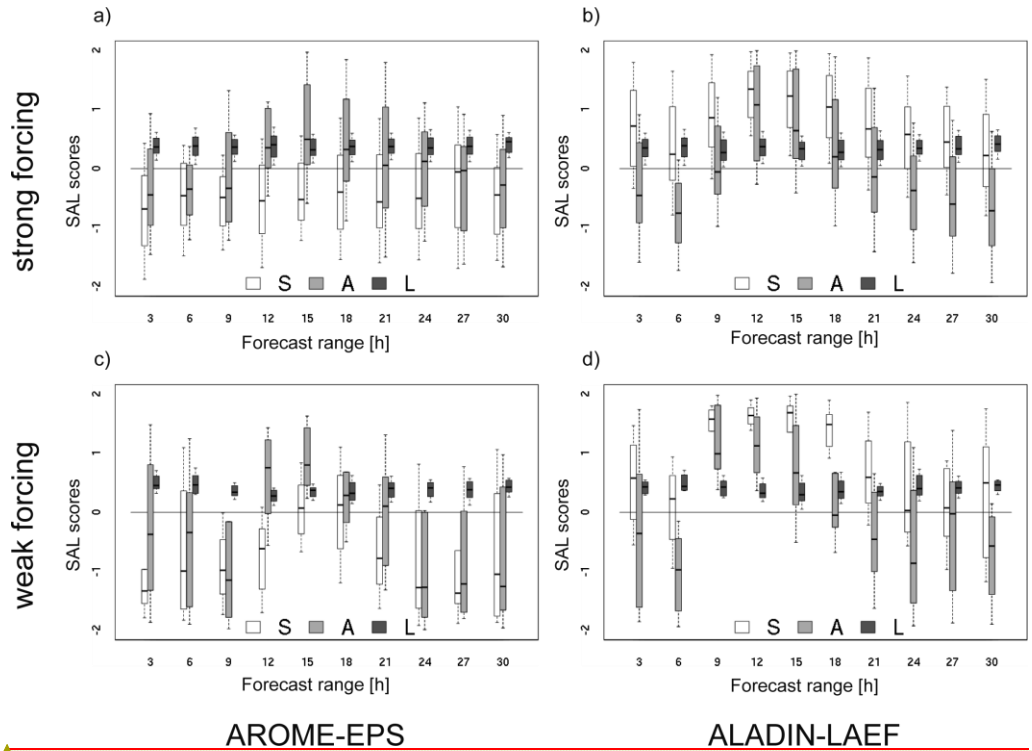
1205

1206 Figure 6: Time evolution of the Brier Score with confidence intervals (shades) for
 1207 region *Austria*, AROME-EPS (dotted line) and ALADIN-LAEF (dashed line). a) strong
 1208 synoptic forcing and precipitation threshold 0.1 mm / 3 h, b) weak synoptic forcing
 1209 and 0.1 mm / 3 h, c) strong synoptic forcing and 2 mm / 3 h, and d) weak synoptic
 1210 forcing and 2 mm / 3 h.

1211

1212

1213



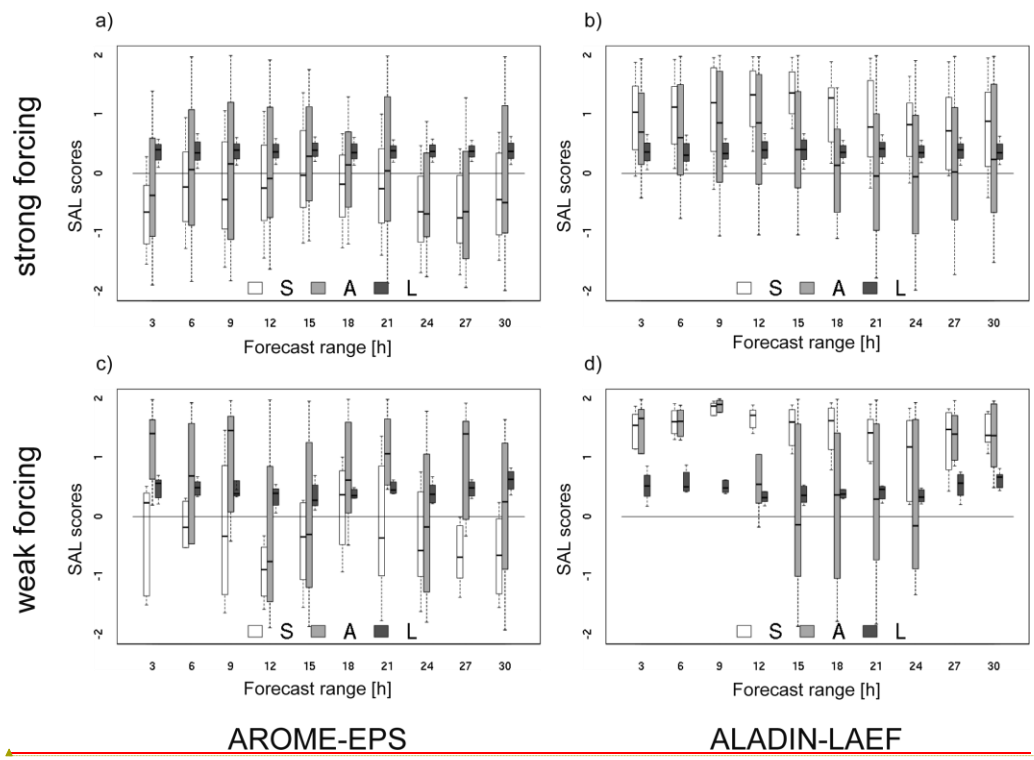
Formatiert: Schriftart: (Standard)
Arial, 12 Pt., Nicht Fett, Schriftartfarbe:
Automatisch

1214

1215 Figure 7: Time evolution of SAL scores for AROME-EPS (left) and ALADIN-LAEF
1216 (right) for different forecast ranges in region West. Upper panels a) and b) show
1217 results for days with strong synoptic forcing; lower panels c) and d) for weak synoptic
1218 forcing. The boxes are created based on the scores of all individual ensemble
1219 members.

1220

1221



Formatiert: Schriftart: 12 Pt.

1222

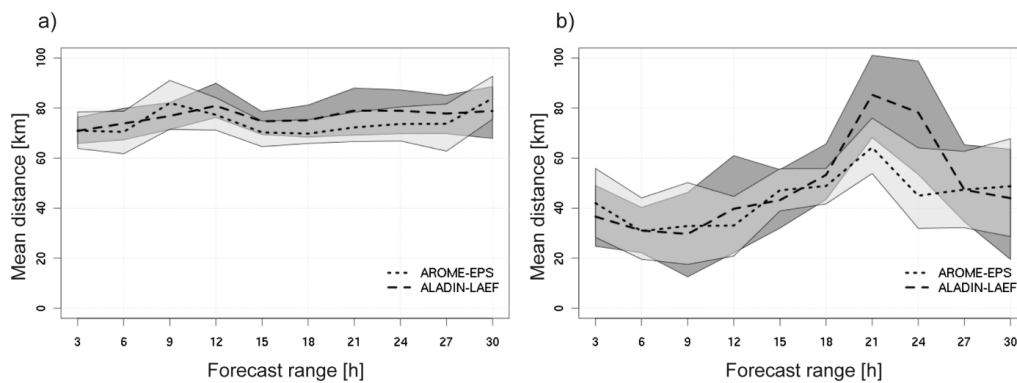
1223

1224

1225

Figure 8: Same as in Figure 7, but for region *Northeast*.

1226



1227

1228 Figure 9: Distances [km] between the centers of mass of the precipitation objects in
1229 the forecast and analysis fields for AROME-EPS (dotted) and ALADIN-LAEF
1230 (dashed) for thresholds of a) 0.1 mm / 3 h, and b) 2 mm / 3 h.

1231

1232

1233

1234

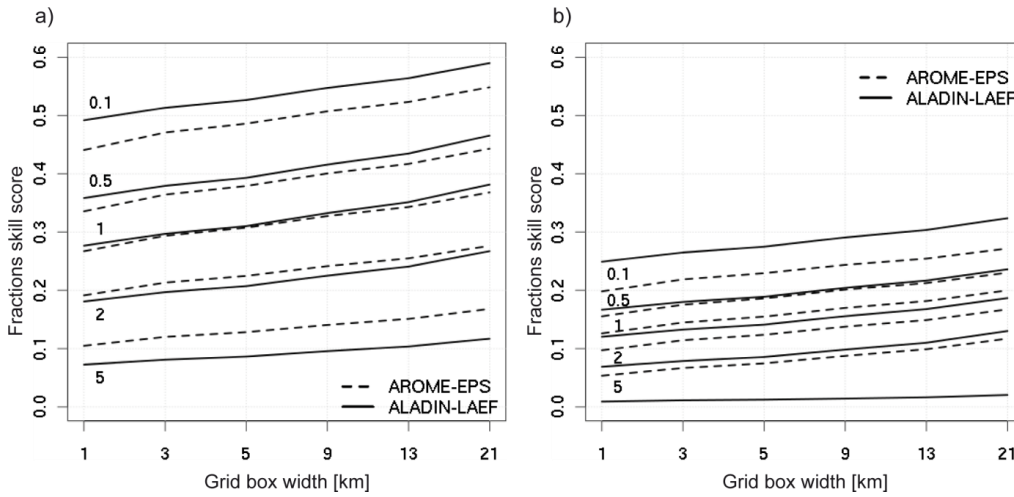
1235

1236

1237

1238

1239



1240

1241 Figure 10: Fractional skill scores for a) strong synoptic forcing, and b) weak synoptic
1242 forcing of AROME-EPS (dashed) and ALADIN-LAEF (solid line) for the region
1243 *Austria*. Numbers denote the precipitation thresholds [mm]. The values represent
1244 averages for all hours of lead-time.

1245

1246

1247

1248

1249

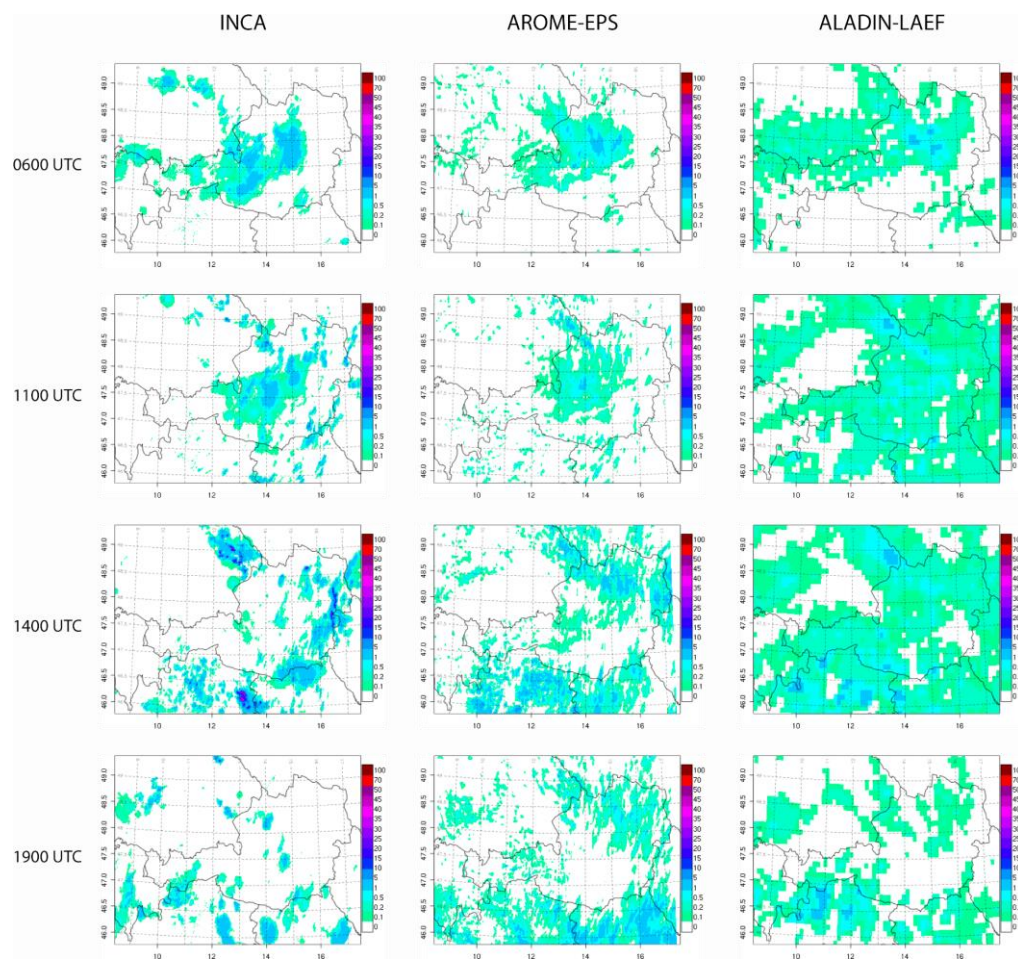
1250

1251

1252

1253

1254

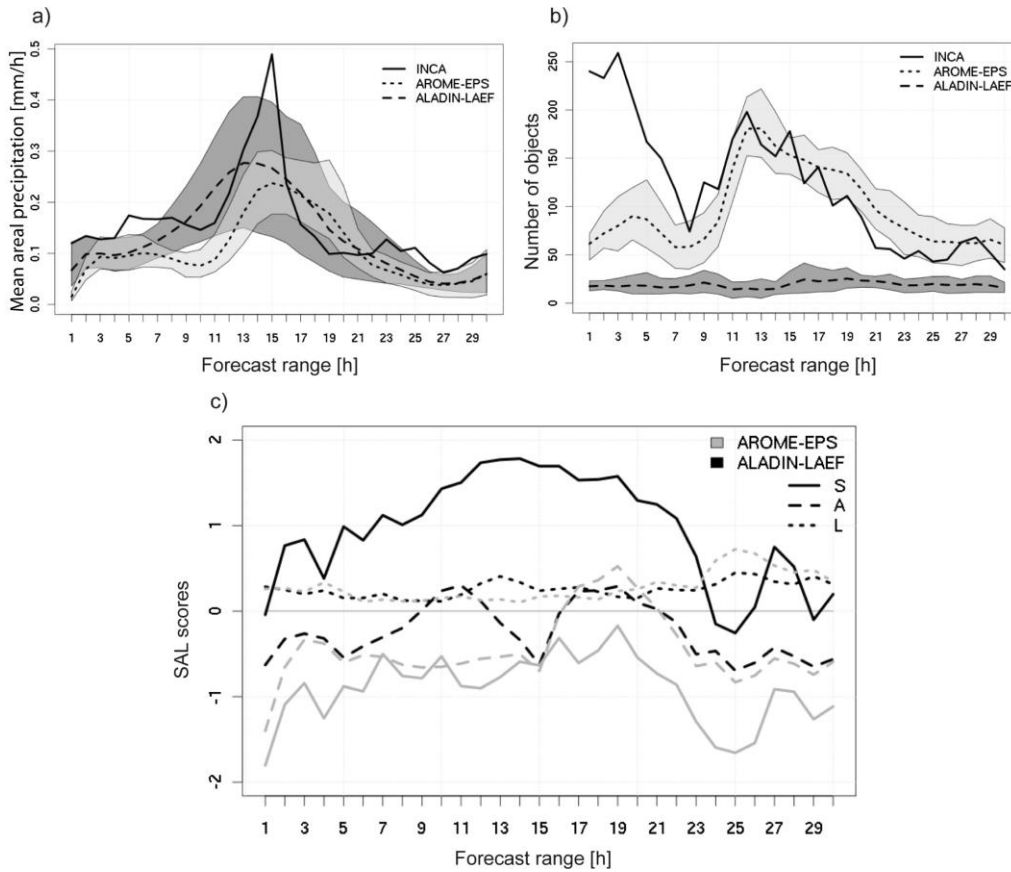


1255

1256 Figure 11: Observed (INCA, first column) and forecast (AROME-EPS and ALADIN-
1257 LAEF, second and third column, respectively) development of precipitation on 29
1258 April 2014 shown for selected times (rows). The panels show 1-hourly accumulated
1259 precipitation sums [mm].

1260

1261



1262

1263 Figure 12: Characteristics of the precipitation forecasts of ALADIN-LAEF and
 1264 AROME-EPS on 29 April 2014. a) Temporal evolution of the mean areal precipitation
 1265 compared with INCA, and b) temporal evolution of the number of precipitation
 1266 objects. Dashed and dotted lines represent the ensemble mean and grey shades the
 1267 ensemble spread. c) Temporal evolution of S (structure), A (amplitude) and L
 1268 (location) scores of the ensemble means of ALADIN-LAEF (black) and AROME-EPS
 1269 (grey).